HYBRID AIR FOIL BEARING WITH EXTERNAL PRESSURIZATION

A Thesis

by

SOONGOOK PARK

Submitted to the Office of Graduate Studies of
Texas A&M University
in partial fulfillment of the requirements for the degree of

MASTER OF SCIENCE

May 2007

Major Subject: Mechanical Engineering

HYBRID AIR FOIL BEARING WITH EXTERNAL PRESSURIZATION

A Thesis

by

SOONGOOK PARK

Submitted to the Office of Graduate Studies of
Texas A&M University
in partial fulfillment of the requirements for the degree of

MASTER OF SCIENCE

Approved by:

Chair of Committee,	Daejong Kim
Committee Members,	Alan Palazzolo
	Wayne N.P. Hung
Head of Department,	Dennis O'Neal

May 2007

Major Subject: Mechanical Engineering

ABSTRACT

Hybrid Air Foil Bearing with External Pressurization. (May 2007)
Soongook Park, B.S., Korea Military Academy
Chair of Advisory Committee: Dr. Daejong Kim

Foil bearings are widely used for oil-free micro turbomachinery. One of the critical technical issues related to reliability of the foil bearings is a coating wear on the top foil and rotor during start/stops. Bearing cooling is also mandatory for certain applications because the foil bearings can generate significant amount of heat depending on operating conditions. Usually axial flow is used through the space between the top foil and bearing sleeve.

In this thesis, a hybrid air foil bearing with external pressurization is introduced. The hybrid operation eliminates the coating wear during start-up/shut down, and also reduces drag torque during starts. Furthermore, this hybrid foil bearing does not need cooling system.

An experimental test with a loaded bearing under hydrostatic mode demonstrates the high potential of hybrid air foil bearings. The load capacity of the hybrid foil bearing was measured at 20,000 rpm, and compared with that of hydrodynamic foil bearing. The hybrid foil bearing has much higher load capacity than the hydrodynamic foil bearing. The starting torque was also measured and compared with hydrodynamic bearing.

A simple analytical model to calculate top foil deflection under hydrostatic pressurization has been developed. Predictions via orbit simulations indicate the hybrid air foil bearings can have a much higher critical speed and onset speed of instability than the hydrodynamic counter part.

Major benefits of the hybrid foil bearings also include very low starting torque, reduced wear of the top foil and rotor, and very effective cooling capability by the pressurized air itself. This new concept of hybrid air foil bearings are expected to be widely applied to the oil free turbomachinery industry, especially for heavily loaded and/or high temperature applications.

DEDICATION

To my God and lovely wife Jeongmin, who have always been there for me and who love me and give their priceless support and encouragement to me.

ACKNOWLEDGMENTS

TABLE OF CONTENTS

Page

LIST OF FIGURES

LIST OF TABLES

NOMENCLATURE

A	Control surface area
A_o	Orifice curtain area (see Fig. 3.3)
C	Norminal clearance
C_d	Discharge coefficient
$c_{Bi,j}$	Equivalent viscous damping coefficient of bump Bi
EI	Bending stiffness of the top foil
$F_{eX,Y}$	Total external forces in X and Y directions
$F_{bX,Y}$	Bearing reaction forces in X and Y directions
F_L	Force acting on torque bar
$f_{Bi,j}$	The total pressure force on a bump with index
h	Local film thickness
$k_{Bi,j}$	Stiffness coefficient of bump Bi
$\dot{m}_c$	Mass flow rate through an orifice
P	Dimensionless pressure
H	Dimensionless film thickness
W	Dimensionless bump deflection
p	Pressure
$p_{Bi,j}$	Nodal pressures
$q_{Bi,j}(x)$	Pressure distribution
R_g	Gas constant for air
T	Temperature of supplied air
U	Rotor surface speed
$w_{Bi,j}(x)$	Actual top foil deflection
$\delta_{Bi,j}$	Deflection of bump Bi
$v_{Bi,j}(x)$	Top foil sagging function

e	Journal eccentricity
ε	Dimensionless eccentricity ($= e/C$)
τ	Dimensionless time ($= \omega t$)
Z	Dimensionless axial coordinate ($= z/R$)
θ	Angular coordinate ($= x/R$)
Λ	Bearing number
$\dot{M}_s$	Dimensionless mass flow rate on the air supply
μ	Viscosity of air
ω	Angular velocity of rotor
N_b	Number of bump
P_s	Non-dimensional supply pressure
Δx	Distance between computational grid points in circular direction
Δz	Distance between computational grid points in axial direction
γ	Structural loss factor
γ_g	Specific gravity of air ($=1$)
k	Adiabatic number
Γ_s	Feeding parameter
S_f	Sagging factor
R	Bearing radius
R_{im}	Imbalance radius
R_t	Length of torque bar
g	Gravity constance
I_c	Rotational moment of inetia of bearing housing
τ_f	Start torque of hybrid foil gas bearing
ζ	Coordinate which is assigned on top of each bump

Subscripts

R	Right hand side of spring bump
L	left hand side of spring bump

CHAPTER I

INTRODUCTION

Foil bearings are widely used for oil-free micro turbomachinery and have been used in applications including turbo generators, aircraft air cycle machines[1], automobiles, fuel cell micro-gas turbine(MGT) hybrid systems[2], turbochargers and turbo compressors, etc. One of the critical technical issues related to reliability of the foil bearings is a coating wear on the top foil and rotor during start/stops. Especially for heavily-loaded foil bearings, large start torque requires a large drive motor. Bearing cooling is also mandatory for certain applications because the foil bearings can generate a significant amount of heat depending on the operating conditions. Usually axial flow is used through the space between the top foil and bearing sleeve.

Bump foil bearings are the most popular. As seen in the Fig. 1.1, foil gas bearings consist of two parts, the smooth top foil and the corrugated bump foil. When bearings have reached certain speed, the hydrodynamic pressure is generated between the top foil and the rotor. The pressure generated in the air film causes the rotor to lift up. The bump foil supplies support for the top foil and can be tailored for the required stiffness of the bearing.
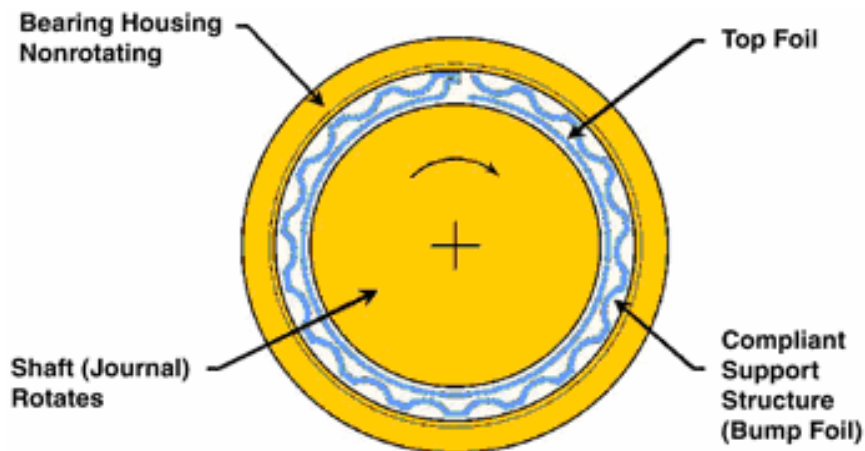
Figure 1.1 Schematic view of foil gas bearing, source from [3]

This thesis follows the style of ASME Journal of Tribology.

However, during start-up and shut-down, the top foil and rotor experiences sliding wear which shortens the average life of the foil bearings.

1.1 Literature Review

Ku and Heshmat [4] developed an analytical model to predict corrugated bump stiffness considering friction force, load distribution, and bump structure, and also measured the structural stiffness as a function of friction coefficients between the contact surfaces and surface conditions [5]. Heshmat and Ku also measured dynamic structural stiffness and equivalent viscous damping comparing with analytical results [6]. Peng and Carpino [7] used perturbation method to calculate dynamic force coefficients of foil bearings. C. Heshmat, Xu, and H. Heshmat [8], calculated load carrying capacity using Finite Difference (FD) and Finite Element (FE) Method for better design of foil bearings. Peng and Khonsari [9] presented thermohydrodynamic analyses on temperature distribution of the air film and compared with experimental results. DellaCorte [10] presented a rule of thumb-based analytical formula predicting comparative load capacities of various air foil bearings, and provides design guidelines of air foil bearing. Kim and San Andrés [11] advanced prediction of load capacities and dynamic force coefficients for heavily-loaded cases using finite element method. They also showed that the load capacity of foil bearings is determined by the structural deflection of support structure and relatively independent of rotor speed. Kim [12] performed parametric studies on the load capacity and stability of two different types of air foil bearings with identical average stiffness and damping of underlying structure, i.e., circular air foil bearing with single top foil and three-pads (top foils) with hydrodynamic preload. Kim [12] shows that the major difference of rotor-bearing stability comes from overall top foil shape rather than distribution of stiffness and damping over the bearing surface. Researchers in [13] adopt 1-D and 2-D finite element (FE) models to calculate top foil deflections under hydrodynamic pressure. Similar 1-D FE model to the one used in [13] was also developed earlier [14], where they studied static and dynamic performance of air foil bearing for different top foil thicknesses. In these 1-D FE models [13, 14], variation of top foil deflection along axial direction is neglected. Carpino and Talmage [15] developed fully coupled FE model that solves pressure field, top foil, and bump deflection together, considering both membrane and bending effect of the top foil.

Heshmat [16] made a foil bearing model assuming that the top foil is ideal to have high stiffness between neighboring bumps. Carpino [17] developed a model considering top foil as a flat shell and analyzed the membrane effects of the top foil. Researchers [16, 17] mentioned above defined the top foil which does not have either membrane effect or bending and also neglected the sagging effect on the top foil influenced by hydrodynamic pressure.

In experimental aspects, Ruscitto [18] performed tests related to film thickness, load capacity, bearing journal surface, and thermal distortion. He also explained the influences and characteristics of foil bearing performances. Salehi [19] measured the dynamic frictional characteristics between top foil and bump foil and bearing housing. Heshmat [20] demonstrated advanced designs of bump foil bearings with 132,000 rpm and load capacity of about 689kPa (100psi) at 60 krpm. Radil [21] indicated the importance of radial clearance considering structural stiffness and damping. They showed that radial clearance lower than optimum value can lead to thermal runaway and low load capacity, due to high preload from the top foils. Reversely, the bearings with clearance higher than optimum have very small decrease of load capacity without any thermal problems.

Despite extensive research on air foil bearings and successful applications in many oil-free turbomachinery applications at low to intermediate temperature ranges, successful implementation of air foil bearings on high temperature applications such as small gas turbines are very few [22].

Extensive research on low friction coatings at high temperature is underway. NASA [23, 24] has been developing PS 300 series ceramic metal composite coating for high temperature applications since 1995. Mohawk Innovative Technology [25] also developed a series of metal-ceramic composite coatings applied to top foil via thermal spray process. These coatings have shown proven performance at limited temperature ranges depending on the material composition. Because of the limited performance of these solid lubricants, the wear of the top foil and rotor is inevitable during the repeated start and stop cycles, and performance also degrades accordingly.

1.2 Research Objective

This thesis introduces the first prototype of hybrid air foil bearings with a direct air

supply through the orifice attached to the top foil. As its name implies, the hybrid foil bearing adopts advantages of rigid-walled hydrostatic gas bearing and hydrodynamic foil gas bearing. By using external pressurized air, higher load capacity, reliability, and low start friction can be achieved. In addition, adoption of compliant elastic foundation can accommodate misalignment, and provide necessary damping for stable operation. The prototype hybrid air foil bearing developed in this thesis uses the foil gas bearing introduced in [26], which uses multiple compression springs instead of bump foils. Detailed configuration of the hybrid foil bearing will be explained later.

The main purposes of thesis are (1) to develop software to calculate bump deflection under hydrostatic pressurization and to solve pressure distribution under hybrid operation; (2) to investigate rotordynamics behavior of a rotor supported by hybrid air foil bearing using orbit simulations; (3) to measure static performance of the hybrid air foil bearing by measuring load capacity, cooling capacity, and starting torque and comparing to those of hydrodynamic air foil bearings.

CHAPTER II

DESCRIPTION OF HYBRID AIR FOIL BEARING

An initial prototype of the suggested hybrid air foil bearing was constructed using the foil gas bearing with compression springs [26], for proof of concept studies. The bearing uses 24 springs which are inserted along the 24 circumferential directions and give proper stiffness and damping which have a role of corrugated bump foil to the top foil.

Figure 2.1 shows a photo of top foil for the hybrid air foil bearing top foil. Four small stainless steel tubes with inner diameter of 1mm were attached through a flexible rubber tube to the back side of the top foil. The top foil has four air supply holes with diameters of 0.5mm. The orifice holes are located in the middle of top foil in axial direction.

Figure 2.1 Photo of top foil for hybrid air foil bearing

Because the initial studies are focused on the proof of concept at room temperature, epoxy glue was used to attach the air supply tubes. However, at high temperature applications, friction welding or brazing could be used. Figure 2.2 shows a photo of an assembled hybrid air foil bearing. Table 2.1 shows more detailed specifications for the hybrid air foil bearing manufactured for experimental studies to be presented in Chapter IV.
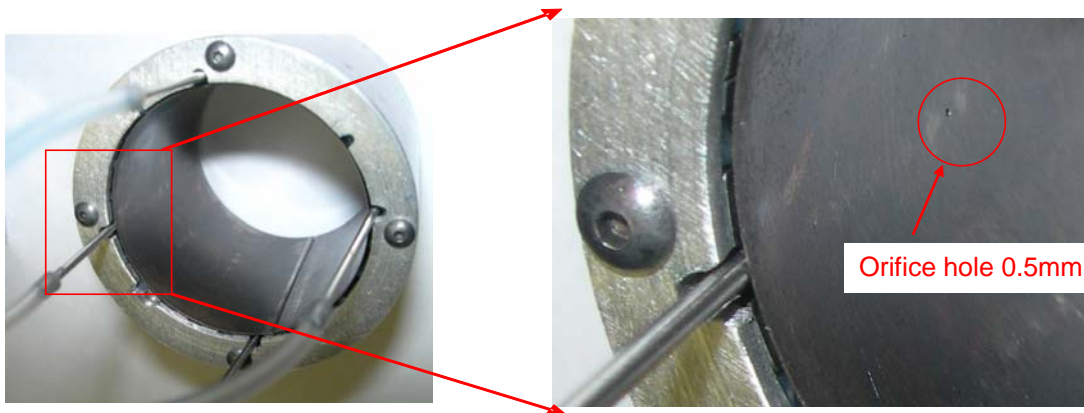
Figure 2.2 Photo of assembled hybrid air foil bearing

Table 2.1 Parameters of manufactured hybrid air foil bearing

Parameters		Values	
Bearing diameter	Inner	38.10 mm	(1.50 inch)
	Outer	50.80 mm	(2.00 inch)
Orifice hole		0.508 mm	(0.02 inch)
Nominal clearance		45.0 μm	(0.00177 inch)
Coating on slots		Diamond-Like Carbon (DLC)	
Number of spring bumps		24	
Spring bump length		30.00 mm	(1.180 inch)
Spring bump pitch		3.33 mm	(0.131 inch)
Spring bump diameter		2.90 mm	(0.114 inch)
Spring wire diameter		0.254 mm	(0.010 inch)
Top foil thickness		0.102 mm	(0.005 inch)
Axial length		30 mm	(1.50 inch)

CHAPTER III

SIMULATION OF HYBRID AIR FOIL BEARING

3.1 Model of Hybrid Bearing

3.1.1 Top Foil Deflection

A new but simple model for top foil deflection has been developed. In a simple approach, each computational grid point is assigned with spring and damper, and deflection of top foil at each nodal point is assumed independent from others (neglecting bending effect of the top foil). In the proposed hybrid air foil bearing, due to the geometrical constraint of the bump foil and air feeding tubes, the air supply orifices are located between the bumps along the circumferential direction. When bending of the top foil is neglected, grid points where hydrostatic orifices are located experience unrealistic top foil deformation and air film thickness. To capture the realistic top foil deflection under these conditions, the new top foil deflection model considers bending moment within the top foil. The model used in this paper uses a simple 1-D analytical beam model as shown in Fig. 3.1 to take elastic bending moment within the top foil into account when calculating top foil deflection. However, membrane effect of the top foil is not considered for simplicity. Unlike 1-D FE models adopted in [13, 14], variation of top foil deflection along the axial direction is implemented by dividing the top foil into multiple top foil segment with the same number as the computational grid points along the axial direction. Therefore, in this model, it is postulated that the deflections of each top foil segment are independent along the axial direction, enabling variable top foil deflections along the axial direction. The total number of the spring bumps along the circumferential direction is 24, and the total number of computational grid points is 48, assigning one computational grid point between adjacent spring bumps.
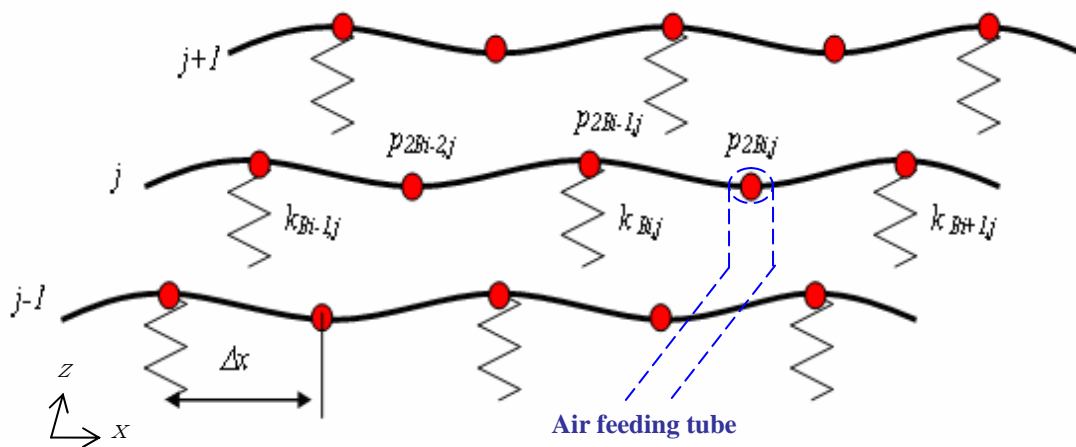
(a) 1-D top foil deflection model; Dots indicate computational nodal points to solve Reynolds Equation
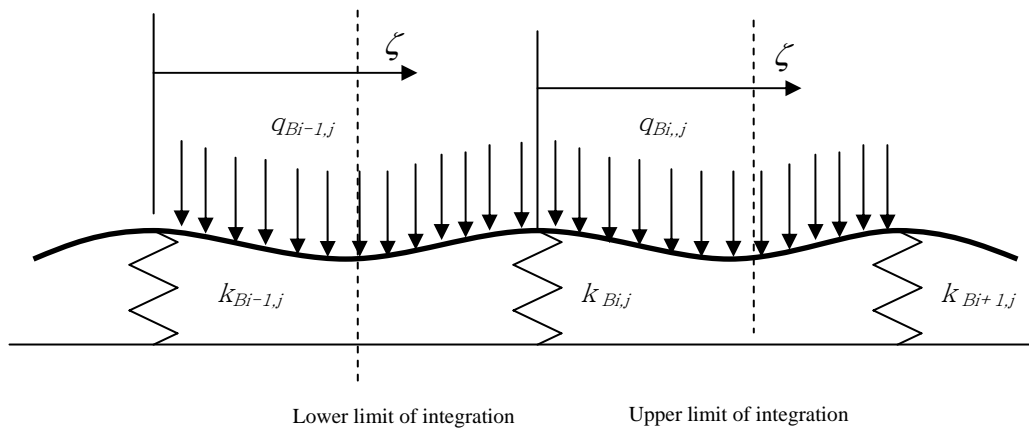
(b) Top foil deflection model under pressure

Figure 3.1 Top foil model considering bending moment along the circumferential direction

Because the number of bumps is 24, computational grid points can be indexed from 0 to 48 as seen in Fig. 3.2. The index, B_i, describes the location of individual bump. If

coordinate ζ is assigned on top of each bump as in Fig. 3.1, the load distribution per unit length $q_{Bi,j}(\zeta)$ on the top foil strip between the bumps B_i and B_{i+1} is assumed to take a parabolic function decided by nodal pressures $p_{2Bi-1,j}$, $p_{2Bi,j}$, and $p_{2Bi+1,j}$;

$$q_{Bi,j}(\zeta) = \left(a_{Bi,j}\zeta^2 + b_{Bi,j}\zeta + c_{Bi,j}\right)\Delta z,$$ (1)

where

$$a_{Bi,j} = \frac{p_{2Bi+1,j} - 2p_{2Bi,j} + p_{2Bi-1,j}}{2\Delta x^2}$$ (2a)

$$b_{Bi,j} = \frac{4p_{2Bi,j} - p_{2Bi+1,j} - 3p_{2Bi-1,j}}{2\Delta x}$$ (2b)

$$c_{Bi,j} = p_{2Bi-1,j}$$ (2c)
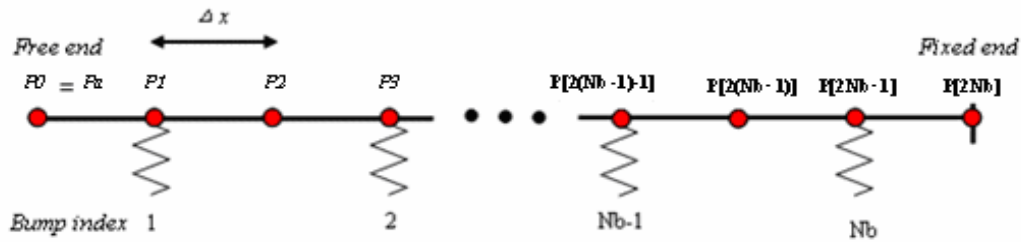
Figure 3.2 Computational grid points on top foil model along the circumferential direction

Therefore, for bump B_i, nodal pressures $p_{2Bi-1,j}$, $p_{2Bi,j}$, and p_{2Bi+1} are used to define the load distribution function $q_{Bi,j}(\zeta)$. The total pressure force $f_{Bi,j}$ on a bump B_i can be calculated by integration of Eq. (1) over the bump pitch between dotted lines in Fig. 3.1(b)

$$f_{Bi,j} = \left(\int_{\Delta x}^{2\Delta x} q_{Bi-1,j}(\zeta)d\zeta + \int_0^{\Delta x} q_{Bi,j}(\zeta)d\zeta\right)\Delta z$$
$$= \frac{1}{12}\left(-p_{2Bi-2,j} + 13p_{2Bi-1,j} + 13p_{2Bi,j} - p_{2Bi+1,j}\right)\Delta z$$ (3)

Here, the $f_{Bi,j}$ is a pressure force on the bump B_i.

Each top foil segment is modeled as a slender beam with clamped ends at both sides but free to move along the horizontal direction as in Fig. 3.2. The linear interpolation function for the total top foil deflection at ζ is defined as

$$w_{Bi,j}(\zeta) = \left(1 - \frac{\zeta}{2\Delta x}\right)\delta_{Bi,j} + \frac{\zeta}{2\Delta x}\delta_{Bi+1,j} + v_{Bi,j}(\zeta), \tag{4}$$

where $\delta_{Bi,j}$ is a deflection of bump B_i and $v_{Bi,j}(\zeta)$ is a sagging term of top foil (called "sagging function" hereafter) at ζ.

To find $v_{Bi,j}(\zeta)$, it is assumed that all the bumps are rigid (i.e. $\delta_{Bi,j}=0$). Then, the sagging function can be found by solving the following equation with zero deflections and slopes at both ends [27]; i.e.,

$$EIv_{Bi,j}''''= q_{Bi,j}(\zeta) \tag{5a}$$

$$v_{Bi,j}(0) = v_{Bi,j}(2\Delta x) = 0 \tag{5b}$$

$$v'_{Bi,j}(0) = v'_{Bi,j}(2\Delta x) = 0, \tag{5c}$$

where EI is a bending stiffness of the top foil and Δx corresponds to the distance between computational grid points along the circumferential direction. Equation (5a) is integrated four times to obtain the sagging function $v_{Bi,j}(\zeta)$. Applying the two boundary conditions, Eqs. (5b) and (5c), the sagging function becomes

$$v_{Bi,j}(\zeta) = -\frac{\Delta z}{EI}\left(\left(-\frac{\zeta^6}{360} + \frac{L^3\zeta^3}{90} - \frac{L^4\zeta^2}{120}\right)a_{Bi,j} + \left(-\frac{\zeta^5}{120} + \frac{L^2\zeta^3}{40} - \frac{L^3\zeta^2}{60}\right)b_{Bi,j} + \left(-\frac{\zeta^4}{24} + \frac{L\zeta^3}{12} - \frac{L^2\zeta^2}{24}\right)c_{Bi,j}\right) \tag{6}$$

Once the sagging function $v_{Bi,j}(\zeta)$ is calculated, the sagging amount of top foil at the mid point between two adjacent bumps can be evaluated as

$$v_{Bi,j}(\Delta x) = \frac{\Delta x^4 \Delta z}{120EI}\left(3p_{2Bi+1,j} + 3p_{2Bi-1,j} - p_{2Bi,j}\right) \tag{7}$$

The bump deflection term $\delta_{Bi,j}$ in Eq. (4) can be found from the following bump dynamic equation

$$f_{Bi,j} = k_{Bi,j}\delta_{Bi,j} + c_{Bi,j}\dot{\delta}_{Bi,j}, \tag{8}$$

where $k_{Bi,j}$ and $c_{Bi,j}$ are bump stiffness and equivalent viscous damping coefficients, respectively. The equivalent bump viscous damping coefficient $c_{Bi,j} = \gamma\dfrac{k_{Bi,j}}{\omega_s}$, from equivalent damping energy dissipation for one cycle through structural loss factor γ of the bump. The $f_{Bi,j}$ is given by Eq. (3). Once the bump deflection $\delta_{Bi,j}$ are known, the total top foil deflection can be calculated by the following equations.

$$\text{At } \zeta=0, \quad w_{Bi,j}(0) = \delta_{Bi,j} \tag{9a}$$

$$\text{At } \zeta=2\Delta x, \quad w_{Bi,j}(2\Delta x) = \delta_{Bi+1,j} = \delta_{Bi+1,j} \tag{9b}$$

$$\text{At } \zeta=\Delta x, \quad w_{Bi,j}(\Delta x) = \frac{1}{2}\delta_{Bi,j} + \frac{1}{2}\delta_{Bi+1,j} + v_{Bi,j}(\Delta x) \tag{9c}$$

As Eq. 9(c) states, the top foil deflection at the mid point between bumps is assumed to be an average of two adjacent bump deflections plus sagging term given by Eq.(7).

Equation (7) can be non-dimensionalized as

$$V_{Bi,j}(R\Delta\theta) = \frac{v_{Bi,j}}{C}(R\Delta\theta) = \frac{R^5 p_a}{120EIC}\left(3P_{2Bi+1,j} + 3P_{2Bi-1,j} - P_{2Bi,j}\right)\Delta\theta^4\Delta Z, \tag{10}$$

where

$$P = p/p_a \tag{11a}$$

$$\Delta\theta = \Delta x/R \tag{11b}$$

$$\Delta Z = \Delta z/R \tag{11c}$$

$$\tau = \omega t \tag{11d}$$

Here p_a is atmospheric pressure and R is the bearing radius. Equation (8) can also be non-dimensionalized as

$$f_{Bi,j} = \overline{P}_{Bi,j} A_0 = k_{Bi,j} C D_{Bi,j} + c_{Bi,j} C \omega \frac{dD_{Bi,j}}{d\tau}, \qquad (12)$$

where A_0 is an area that the bump B_i covers and $\overline{P}_{Bi,j}$ is average pressure applied over the area A_0. By adopting the following non-dimensional parameters

$$K_{Bi,j} = \frac{k_{Bi,j} C}{p_a A_0}, \qquad (13a)$$

$$C_{Bi,j} = \frac{c_{Bi,j} C \omega}{p_a A_0}, \qquad (13b)$$

$$\overline{P}_{Bi,j} = \frac{\overline{p}_{Bi,j}}{p_a}, \qquad (13c)$$

Eq. (12) can be written as

$$\overline{P}_{Bi,j} = K_{Bi,j} D_{Bi,j} + C_{Bi,j} \frac{dD_{Bi,j}}{d\tau} \qquad (14)$$

To obtain the proper non-dimensional pressure on the top foil for modeling, it is necessary to find correct pressure forces on both the first bump and last bump. At the first bump, as shown in Fig. 3.2, pressure from the free end of the top foil to the first bump is assumed linear. Therefore, pressure force at the first bump is evaluated as

$$\begin{aligned} f_{1,j} &= \int_0^{\Delta x} q_{1,j}(\zeta) d\zeta + \frac{p_{1,j} + p_a}{2} \Delta x \Delta z \\ &= \frac{1}{12}\left(-p_{3,j} + 8p_{2,j} + 11p_{1,j} + 6\right)\Delta x \Delta z \qquad (15) \\ &= \overline{p}_{1,j} \Delta x \Delta z \end{aligned}$$

The non-dimensional pressure at the first bump becomes

$$\overline{P}_{1,j} = \frac{1}{12}\left(-P_{3,j} + 8P_{2,j} + 11P_{1,j} + 6\right) \tag{16}$$

Considering that the end of top foil is fixed, as shown in Fig. 3.2, the pressure from the last bump to fixed end is assumed equal to the pressure on the last bump. Therefore, the pressure force at the last bump can be presented as follows:

$$\begin{aligned}
f_{Nb,j} &= \int_{\Delta x}^{2\Delta x} q_{Nb-1,j}(\zeta)d\zeta + \frac{p_{2Nb-1,j} + p_a}{2}\Delta x\Delta z \\
&= \frac{1}{12}\left(-p_{2Nb-2,j} + 20p_{2Nb-1,j} + 5p_{2Nb,j}\right)\Delta x\Delta z \\
&= \overline{P}_{Nb,j}\Delta x\Delta z,
\end{aligned} \tag{17}$$

The non-dimensional pressure at the last bump becomes

$$\overline{P}_{Nb,j} = \frac{1}{12}\left(-P_{2Nb-2,j} + 20P_{2Nb-1,j} + 5P_{2Nb,j}\right) \tag{18}$$

3.1.2 Hydrostatic Air Supply

Applying a mass continuity equation including a control volume with the external pressurized air supply sources as seen in Fig. 3.3, the Reynolds Equation for a compressible fluid becomes

$$\nabla\left(-\frac{1}{12\mu}ph^3\,\nabla p\right) + \frac{U}{2}\frac{\partial(ph)}{\partial x} + \frac{d(ph)}{dt} = \frac{R_g T\dot{m}_s}{A}, \tag{19}$$

where p is a pressure, μ is a viscosity, U is a rotor surface speed, h is a local film thickness, R_g is a gas constant for air, T is a temperature of supplied air, and A is the control surface area defined as $A=\Delta x\Delta z$. The ∇ is a gradient operator. In order to get the $\dot{m}_s$, a widely used

isotropic process for compressible gas flow model through an orifice [28] is adopted with discharge coefficient C_d.

$$\dot{m}_s = \frac{p_s}{\sqrt{R_g T_s}} C_d A_o \left[2\gamma_g \frac{k}{k-1} \left(\left(\frac{p}{p_s} \right)^{2/k} - \left(\frac{p}{p_s} \right)^{(k+1)/k} \right) \right]^{1/2} \qquad \frac{p}{p_s} < \left(\frac{2}{k+1} \right)^{k/(k-1)} \quad (20a)$$

$$\dot{m}_s = \frac{p_s}{\sqrt{R_g T_s}} C_d A_o \left(2\gamma_g \frac{k}{k+1} \right)^{1/2} \left(\frac{2}{k+1} \right)^{1/(k-1)} \qquad \frac{p}{p_s} > \left(\frac{2}{k+1} \right)^{k/(k-1)} , (20b)$$

where $A_o = \pi d_o h$ is an effective orifice area (not actual orifice hole area on the top foil) and C_d is a discharge coefficient. Equations (20a) and (20b) correspond to the unchoked and choked conditions, respectively.

Non-dimensionalizing Eq. (19) and applying divergence theorem to the first two terms on the left hand side yields

$$\begin{aligned}
&\left(-H^3 P \frac{dP}{d\theta} + \Lambda PH \right)_{out} \Delta Z - \left(-H^3 P \frac{dP}{d\theta} + \Lambda PH \right)_{in} \Delta Z + \\
&\left(-H^3 P \frac{dP}{dZ} \right)_{out} \Delta\theta - \left(-H^3 P \frac{dP}{dZ} \right)_{in} \Delta\theta + 2\Lambda\Delta\theta\Delta Z \frac{d(PH)}{d\tau} = \dot{M}_s
\end{aligned} \qquad (21)$$

where θ is angular coordinate, Z is axial coordinate ($= z/R$) and bearing number Λ is defined as

$$\Lambda = \frac{6\mu\omega}{p_a} \left(\frac{R}{C} \right)^2 \qquad (22)$$
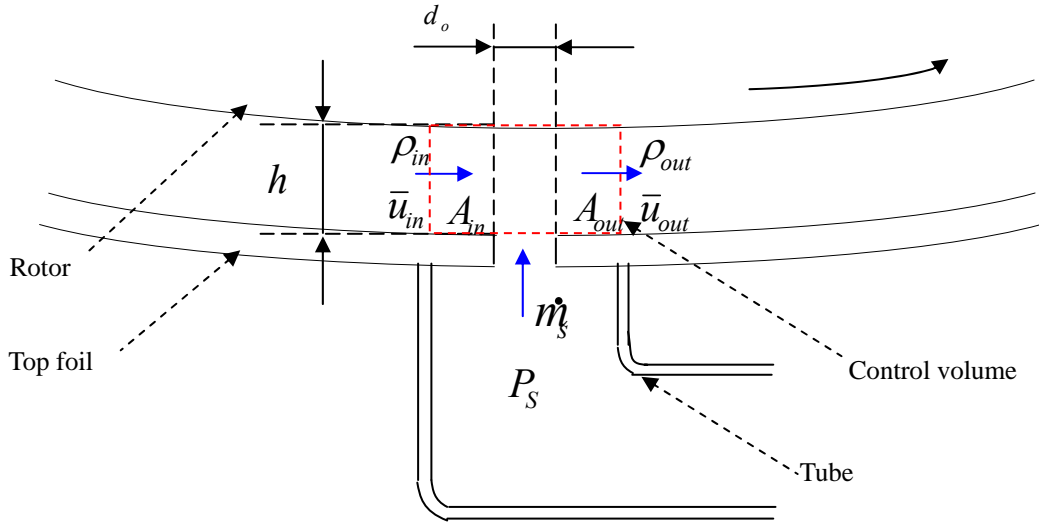
Figure 3.3 Schematics of air supply

The right hand side of Eq.(21), $\dot{M}_S$, can be represented by

$$\dot{M}_s = \frac{12\mu R_g T}{p_a^2 C^3}\dot{m}_s = \Gamma_s P_s H \left[2\gamma_g \frac{k}{k-1}\left(\left(\frac{p}{p_s}\right)^{2/k} - \left(\frac{p}{p_s}\right)^{(k+1)/k} \right) \right]^{1/2} \qquad (23a)$$

$$\dot{M}_s = \frac{12\mu R_g T}{p_a^2 C^3}\dot{m}_s = \Gamma_s P_s H \left(2\gamma_g \frac{k}{k+1} \right)^{1/2} \left(\frac{2}{k+1} \right)^{1/(k-1)}, \qquad (23b)$$

where feeding parameter Γ_s is defined as

$$\Gamma_s = \frac{12\mu C_d A_0 \sqrt{R_g T}}{p_a C^3} \qquad (24)$$

The general tendency of stability of hydrostatic gas bearings can be affected by two factors. The first priority is smaller bearing clearance and the second is small discharge area to minimize air hammering effect (or transport delay). Cautions related to computer coding is that physical area of one control surface surrounded by grid points should be much larger than air discharge area to have physically meaningful model as shown in Fig. 3.4.
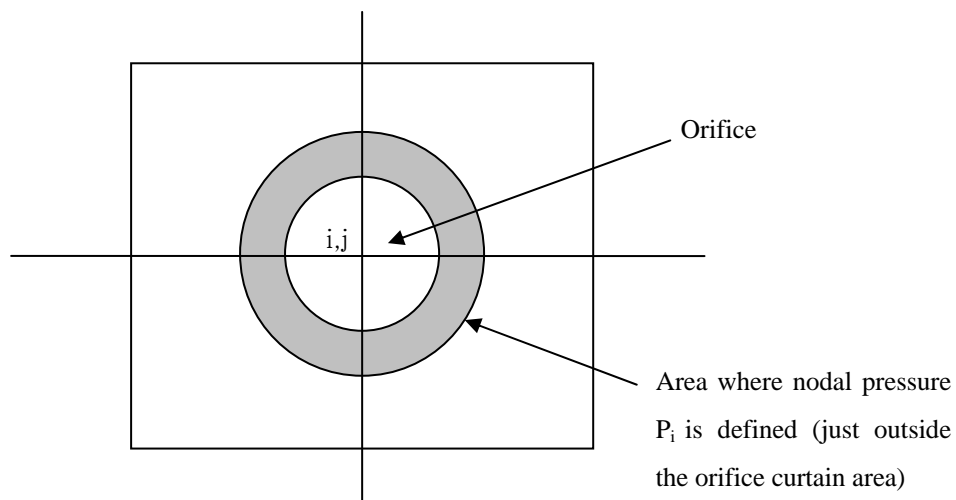

Orifice

Area where nodal pressure P_i is defined (just outside the orifice curtain area)

Figure 3.4 Nodal point with supply air supply pressure

3.1.3 Orbit Simulation

Orbit simulation method developed for air foil bearings [26] was used to characterize the overall performance. Detailed procedure of the orbit simulations can be found in [26]. The orbit simulation procedure is briefly reviewed. In the orbit simulation, the trajectory of rotor center, Reynolds Equation, and bump dynamics (Eq. 14) are solved in time domain simultaneously. For coordinate system shown in Fig. 3.9, the non-dimensional local film thickness from Fig. 3.5 is determined by

$$H = 1 + \varepsilon_X \cos\theta + \varepsilon_Y \sin\theta + W(\theta, Z), \tag{25}$$

where ε $(=e/C)$ is eccentricity from bearing center, $W(\theta,Z)$ is a local bump deflection normalized by nominal bearing clearance, C.
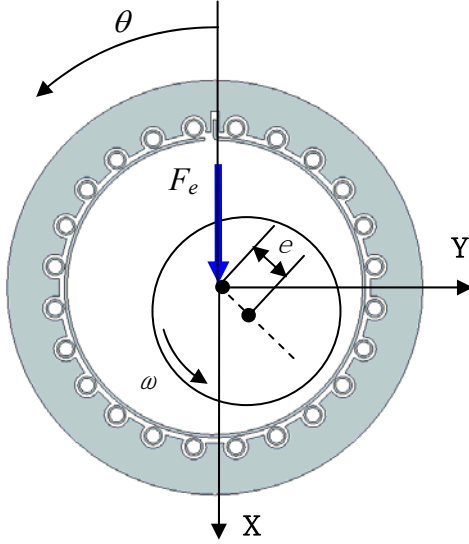

Figure 3.5 Geometry of air foil bearing with springs

The rotor equations of motion are given by

$$m_r C\omega^2 \frac{d^2\varepsilon_X}{d\tau^2} = F_{bX} + F_{eX} \tag{26a}$$

$$m_r C\omega^2 \frac{d^2\varepsilon_Y}{d\tau^2} = F_{bY} + F_{eY}, \tag{26b}$$

where m_r is a rotor mass, R_{im} is an imbalance radius, g is a gravity constant, F_{eXY} are external load applied to the bearing, and F_{bXY} are bearing reaction forces given by

$$F_{bX} = -p_a R^2 \int_0^{2\pi} \int_0^{L/R} P(\theta,Z-1)\cos\theta \ d\theta \ dZ \tag{27c}$$

$$F_{bY} = -p_a R^2 \int_0^{2\pi} \int_0^{L/R} P(\theta,Z-1)\sin\theta \ d\theta \ dZ \tag{27d}$$

A fifth order Adams-Bashforth [29] scheme was used for numerical integration of Eq.(26). State variables for the first five time steps were calculated using a fourth order Runge Kutta method.

3.2 Model Validation

The top foil sagging term, Eq. 7, from the 1-D analytical beam model is the maximum allowable deflection when each bump is modeled as point support. However, as described in Fig. 3.6, actual top foil sagging term can be much smaller than the calculation based on the 1-D analytical beam model because actual contact area between the top foil and bump can be much larger. The top foil can be much stiffer than the model especially when the bearing is heavily-loaded because the effective contact area between the top foil and bump increases. To compensate the uncertainty involved in the complicated interactions between top foil and bump foil, appropriate sagging factor (less than 1), S_f, was sought via comparison between analytical results from the proposed model and experimental data available from NASA [18].
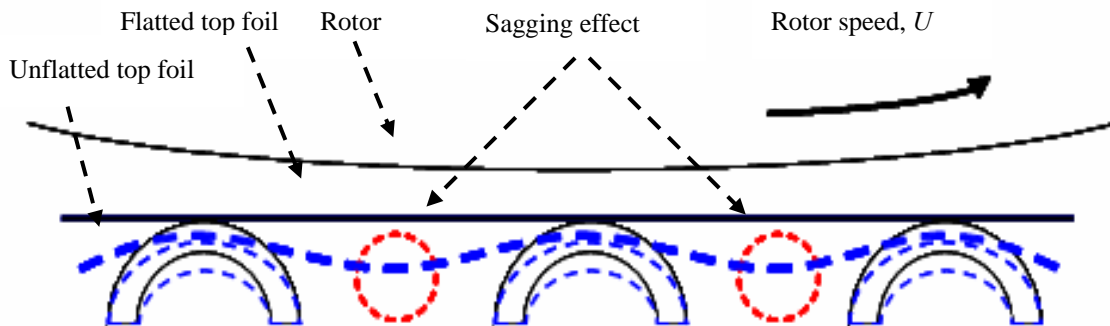

Figure 3.6 Schematic view of top foil and bump deflection

To find the appropriate sagging factor, model simulations were performed using the bearing parameters in reference [18]. Table 3.1 provides the parameters in [18]. The bump stiffness in Table 3.1 is the theoretical value for free-free case [30].

Table 3.1 Hydrodynamic air foil bearing parameters [18]

Parameters	Values	
Inside bearing diameter ($D = 2R$)	38.10 mm	(1.50 inch)
Bearing length (L)	38.10 mm	(1.50 inch)
Nominal clearance (C)	31.8 μm	(0.00125 inch)
Top foil thickness	0.1016 mm	(0.004 inch)
Bump foil thickness	0.1016 mm	(0.004 inch)
Coating on bearing sleeve	Thin hard chromium alloy	
Number of bumps	26	
Bump stiffness per unit area, K	4.7 GN/m^3	
Bump length in circumferential	3.556 mm	(0.140 inch)
Bump pitch	4.572 mm	(0.180 inch)
Bump height	0.508 mm	(0.020 inch)
Shaft speed	30,000 rpm	(3142 rad/s)
Bearing load	134.1 N	

The orbit simulation method can find minimum film thickness for given static load and rotor mass if the method is used without imbalance. Figure 3.7 is the normalized film thickness with maximum allowable sagging effect (S_f=1) when bearing load of 134.1N is applied with no imbalance. As can be seen, the fluctuation of the air film thickness is very large. Figure 3.8 plots the film thickness at the bearing mid plane by applying various sagging factors. As S_f becomes smaller, film thickness in heavily loaded zone (120 to 240 degree) becomes smooth.
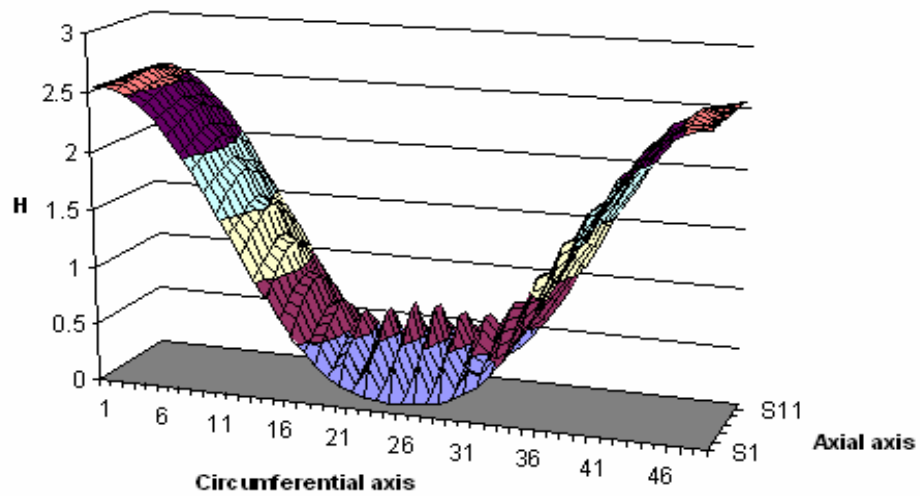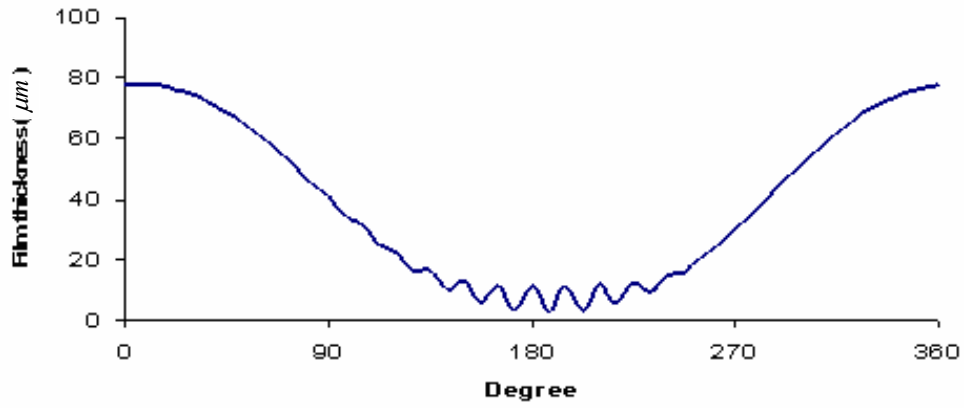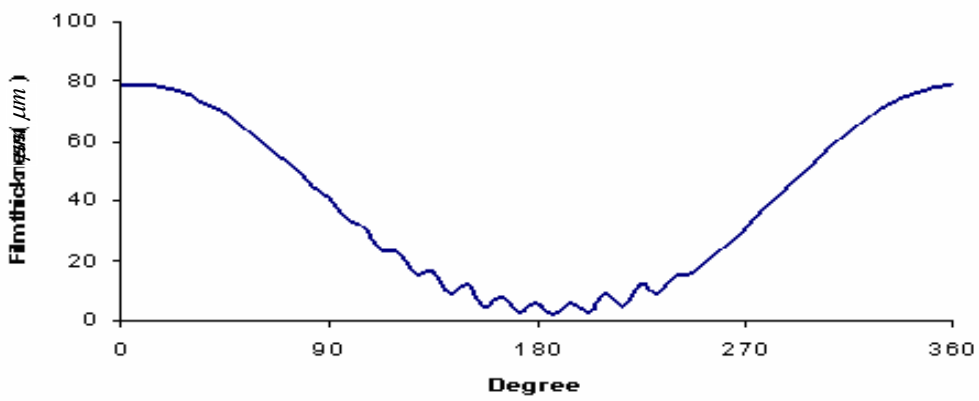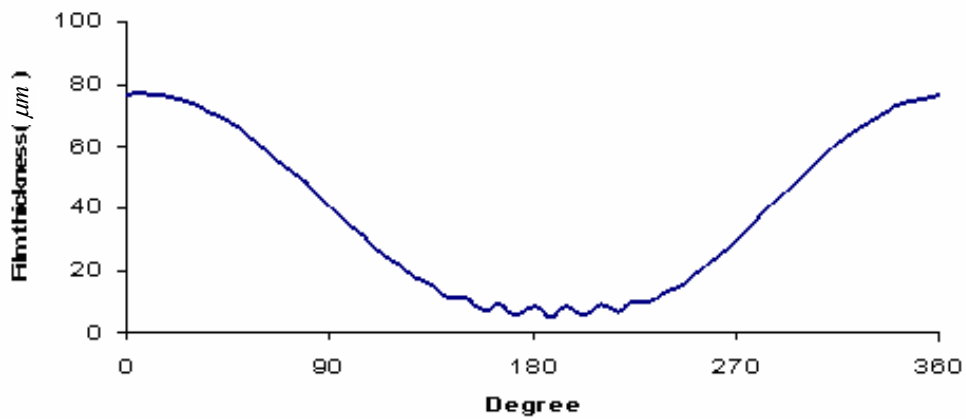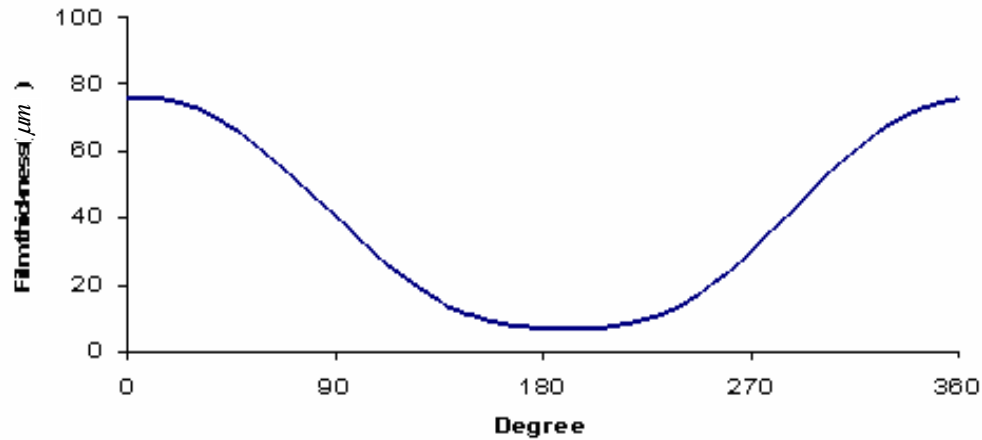
Figure 3.7 Non-dimensional film thickness for operating parameters in Table 3.1 with
$S_f=1$

(a) $S_f = 0.8$

(b) $S_f = 0.5$

(c) $S_f = 0.2$

Figure 3.8 Analytical film thickness with S_f = 0.8, 0.5, 0.2, and 0

with external load of 134.1N

(d) $S_f = 0$

Figure 3.8 Continued

Figure 3.9 compares analytical air film thickness for the operating parameters in Table. 3.1 with S_f=0.2 with experimental test data presented in [18]. In heavily loaded case, the analytical data with sagging factor, $S_f = 0.2$, matches very well with test data result [18]. As a result, sagging factor of 0.2 was applied to the proposed 1-D analytical beam model for analytical results of hybrid air foil bearings presented in this thesis.

Further verification of the model was performed by comparing analytical results of minimum film thickness for the bearing parameters in Table 3.1. External load was varied from 41.1~200.4N and test speeds were 30,000 rpm and 45,000 rpm. Figure 3.10 compares predicted minimum film thickness with measured minimum film thickness for two different rotating speeds as a function of applied loads. The simulation results match very well with experimental results, showing high fidelity of the computational method developed.

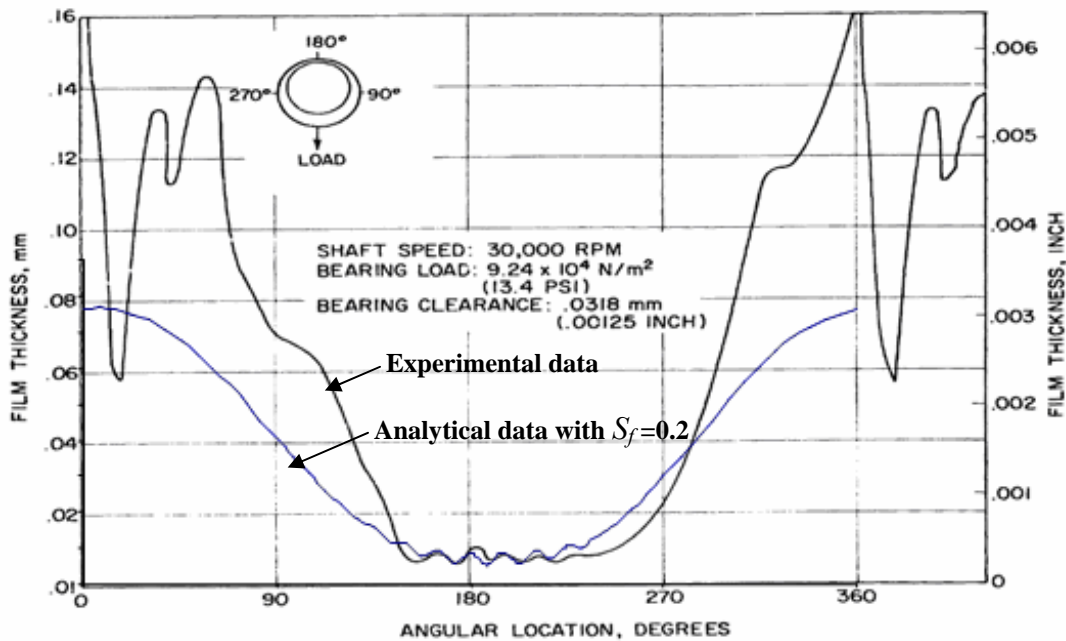**Figure 3.9 Analytical film thickness comparing with test result [18]**
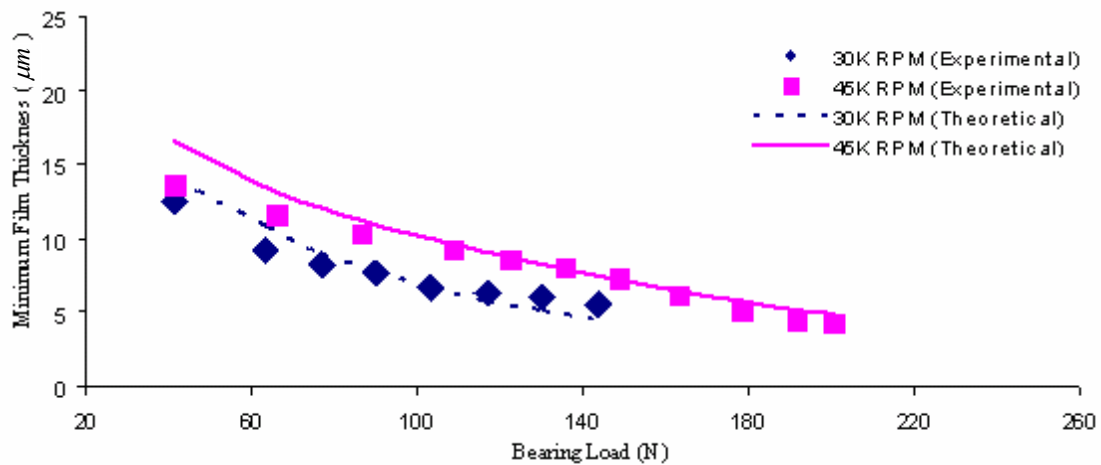
Figure 3.10 Computer predicted and NASA [18] experimental minimum film thickness; L/D=1, C=31.8 μm , and bump stiffness = 4.7 GN/m^3

Figure 3.11 describes a non-dimensional pressure ($P=p/p_a$), film thickness ($H=h/C$), and bump deflection ($W=w_B/C$) for the bearing in Table 3.1 at 45,000 rpm under external load of 145N.

(a) Normalized pressure

(b)   Normalized film thickness

(c) Normalized bump deflection
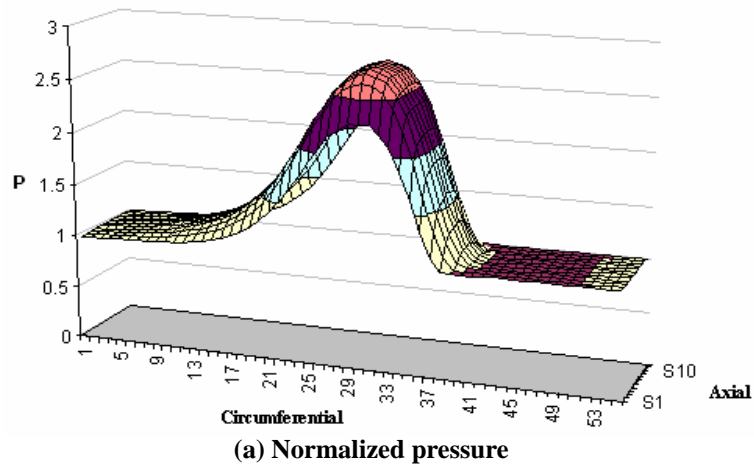
Figure 3.11 Normalized pressure, film thickness, and bump deflection at 45,000 rpm under bearing load 145N, bump stiffness=4.7 GN/m3

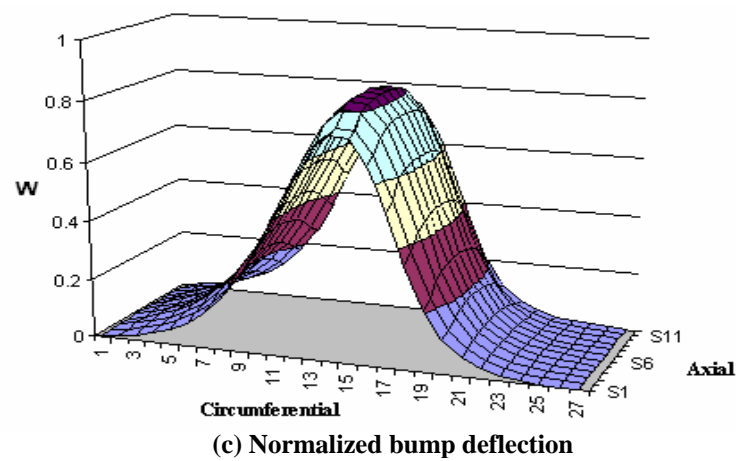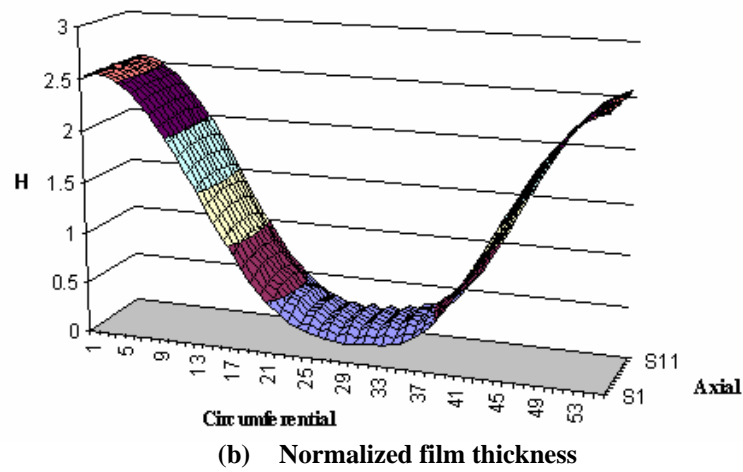Especially for lightly loaded case with sagging effect, Figure 3.12 compares analytical air film thickness for the operating parameters in Table. 3.1 with S_f=0.2 and 0 with external load of 10N. In lightly loaded case, film thickness distribution with $S_f = 0.2$, has similar pattern to that with $S_f = 0$. As a result, sagging effect is negligible in lightly loaded case of hybrid air foil bearings. However, in the forthcoming simulations, sagging factor of 0.2 was applied regardless of the load.

(a) $S_f = 0$

(b) $S_f = 0.2$

Figure 3.12 Analytical film thickness with $S_f = 0.2$ and 0 with external load of 10N

CHAPTER IV

ANALYTICAL PARAMETRIC STUDIES

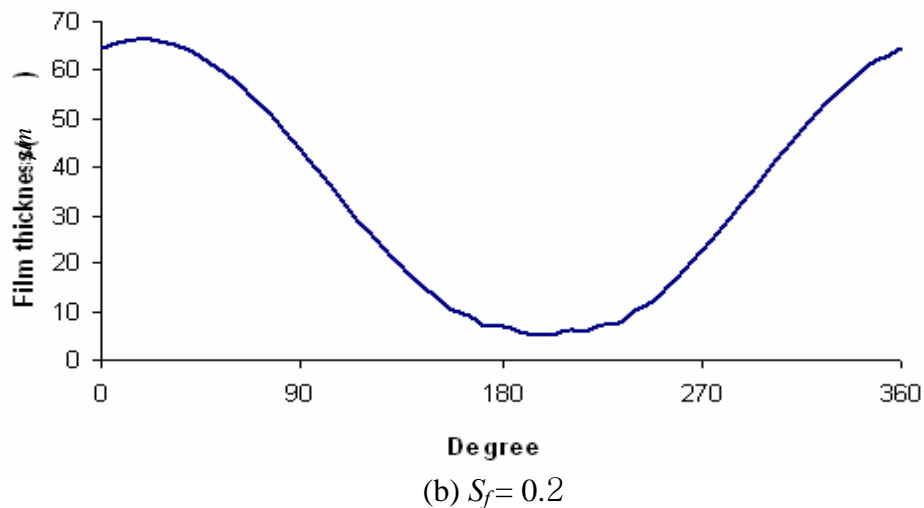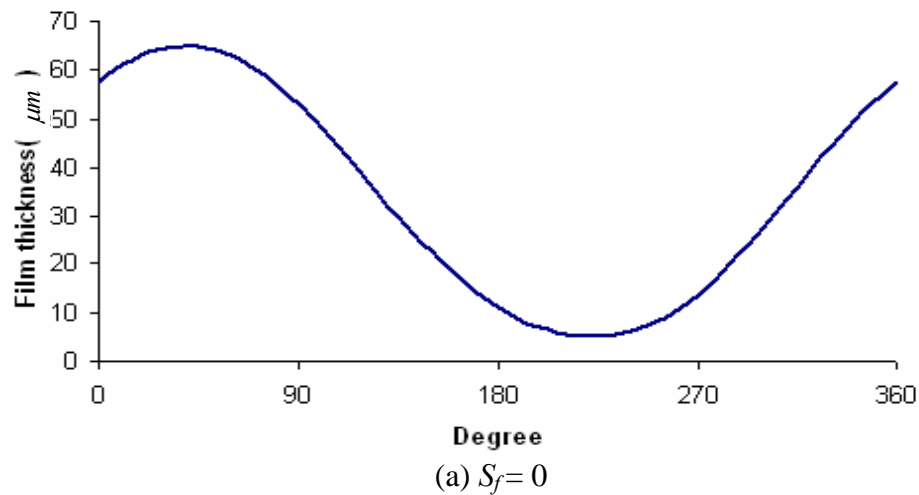Manufactured bearing shown in Fig. 2.2 has individual bump stiffness of about 0.77 GN/m^3. Simulation parameters are given in Table 4.1. For those parameters, detailed simulated hydrodynamic performance was presented in [26] without considering top foil sagging effect. With the same simulation parameters as in [26], dynamic performance of hydrodynamic air foil bearing and hybrid air foil bearings considering with top foil sagging effect are compared with results in [26]. For the simulation, loss factor of 0.25 is assumed for all the bumps.

Table 4.1 Parameters for orbit simulation

Rotor speed, ω	6,000~16,000 rpm (628~1676 *rad/s*)
Bearing diameter($D=2R$)	38.1 mm (R=19.05 mm)
Bearing axial length, L	30 mm
Nominal clearance, C	25 μm
Rotor mass, m_r	0.6 kg
Rotor imbalance, R_{im}	570 mg-mm
External load, F_e	0 N
Spring bump stiffness, K	0.77 GN/m^3,
Structural loss factor, γ	0.25
Top foil thickness	127 μm
Sagging factor, S_f	0.2
Young's modulus (top foil), E	200 GPa

4.1 Effect of Top Foil Sagging on Rotor-Bearing Stability in Hydrodynamic Bearing

Figure 4.1 is selected orbits for hydrodynamic bearing with S_f =0.2. The dotted arcs are the nominal bearing clearance. Fig. 4.2 compares coast down simulation of hydrodynamic bearing with S_f =0.2 and S_f =0. For S_f =0, the critical speed, natural frequency, and OSI are 9,380rpm, 7,495rpm, and 13,942rpm. For S_f =0.2, the critical speed, natural frequency, and OSI are 9,280 rpm, 7,517rpm, and 13,783rpm respectively. Overall responses are very similar and the effect of top foil sagging on the overall rotor bearing characteristics is negligible, especially for lightly-loaded cases.

4.2 Comparison between Hydrodynamic and Hybrid Mode for Different Nominal Clearance

For hydrodynamic bearing, the bearing with smaller clearance (10μm) has higher OSI than the case with larger clearance (25μm), as shown in Fig. 4.3. In the case of C=10μm, OSI is about 15,797 rpm and critical speed is about 13,794 rpm with natural frequency of around 10,526 rpm. The hydrodynamic bearing with smaller clearance has 14.6% higher OSI compared to larger clearance case. Additionally, critical speed and natural frequency are increased 48.6% and 40.0% respectively.
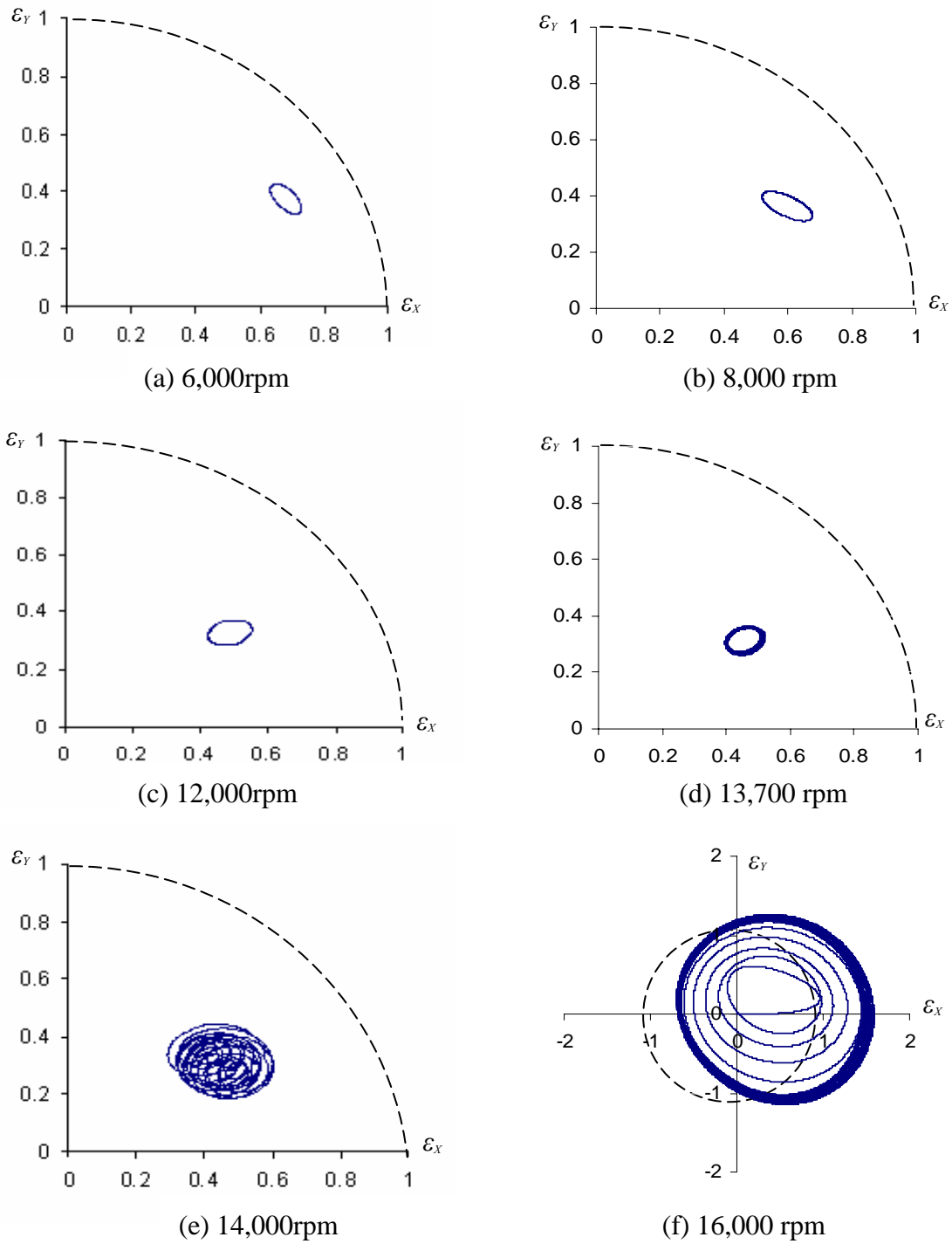
Figure 4.1 Orbits of hydrodynamic air foil bearing; imbalance 570 mg-mm, rotor mass 0.6 *kg*, γ =0.25, S_f =0.2, and bump stiffness = 0.77 GN/m^3
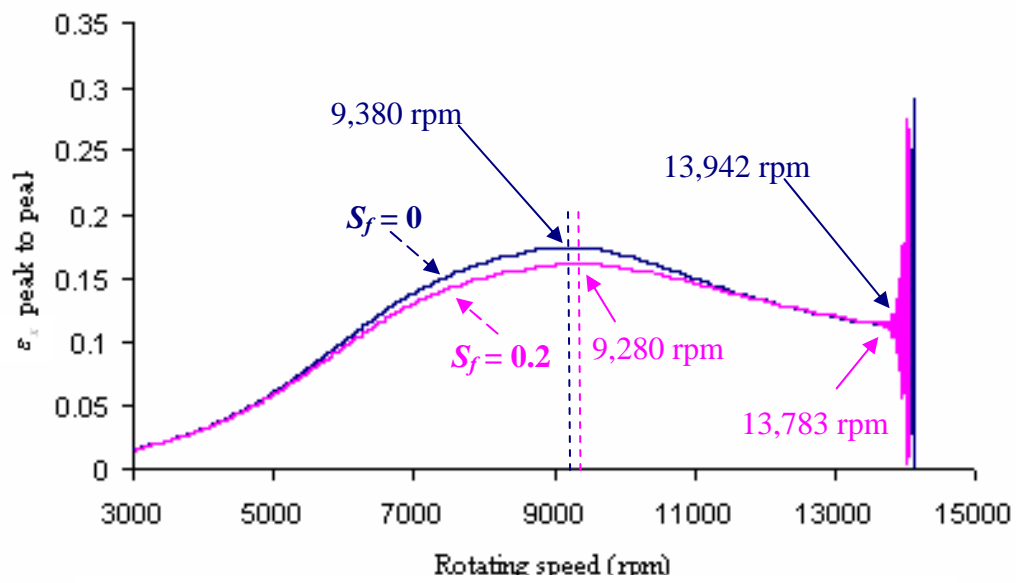
(a) Simulated ε_x peak to peak versus rotating speed
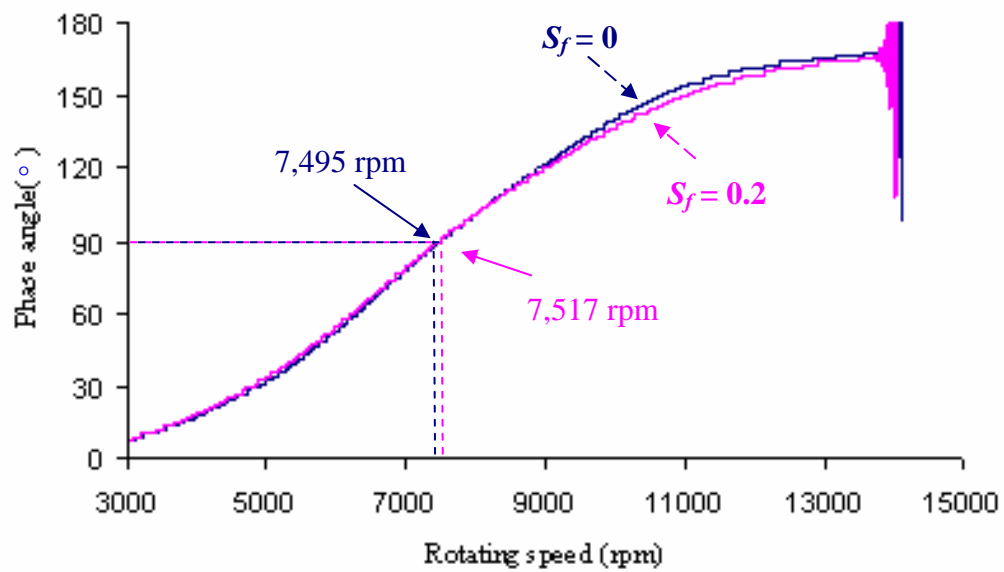
(b) Phase angle versus rotating speed

Figure 4.2 Comparison of analytical ε_x peak to peak and phase angle of rotor-bearing imbalance responses for $S_f=0$ and $S_f=0.2$, bump stiffness = 0.77 GN/m^3

For hybrid bearing, the supply pressure is 400 kPa and orifice diameter on the top foil is 0.5mm for the simulations. For general hydrostatic bearings, it is a common practice to maintain a small bearing clearance to avoid air hammering effect. Hybrid foil bearings suggested in this paper are expected to exhibit similar behavior if the clearance is too large. As shown in Fig. 4.4, the bearing with smaller clearance (10μm) has much higher OSI than the case with larger clearance (25μm). For C=10μm, OSI is about 31,925 rpm and critical speed is about 14,919 rpm with natural frequency of around 14,171 rpm. In case of C=25μm, OSI, critical speed, and natural frequency are reduced to 25,868 rpm, 11,225 rpm, and 11,150 rpm, respectively.

By comparing hybrid operation with C=25μm with the hydrodynamic case with the same clearance (Fig. 4.2), the hybrid air foil bearing has 87.7% higher OSI compared to hydrodynamic bearing. However, critical speed and natural frequency are increased only 20.1% and 48.3% respectively. For C=10μm, OSI increased 102% over hydrodynamic bearing with very similar critical speeds for both cases. Table 4.2 summarizes the results in Figs. 4.3 and 4.4. Apparently, in the case of smaller clearance (10μm), hybrid air foil bearing has much higher OSI than the hydrodynamic bearing. Note the larger clearance is desirable for hydrodynamic bearings for effective bearing cooling. Figure 4.5 shows simulated imbalance responses with 10μm clearance at various speeds.

Table 4.2 Summary of Figs. 4.3 and 4.4   Unit: Rpm

Mode	OSI	Critical Speed	Natural Frequency	Whirl Frequency Ratio (WFR)
Hydrodynamic mode (C=25μm)	13,783	9,280	7,517	0.55
Hydrodynamic mode (C=10μm)	15,797	13,794	10,526	0.67
Hybrid mode (C=25μm)	25,868	11,225	11,150	0.43
Hybrid mode (C=10μm)	31,925	14,919	14,171	0.44
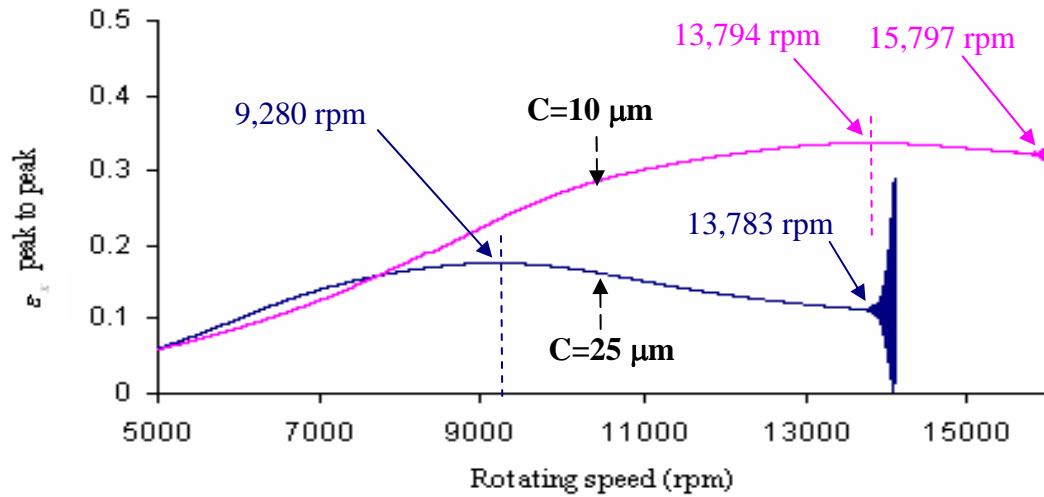
(a) Simulated ε_x peak to peak versus rotating speed
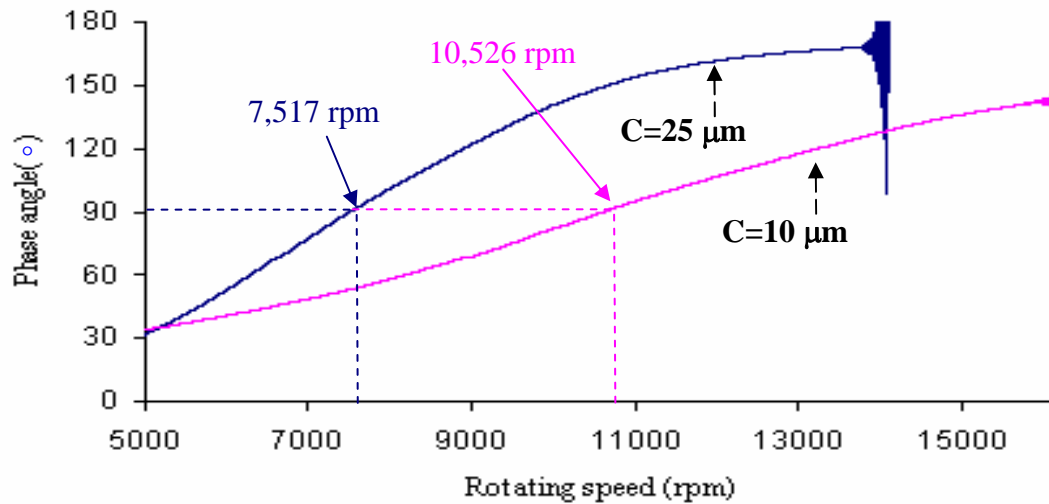
(b) Phase angle versus rotating speed

Figure 4.3 Comparative analytical ε_x peak to peak and phase angle for hydrodynamic bearing with difference bearing clearances; S_f =0.2 and bump stiffness = 0.77 GN/m^3
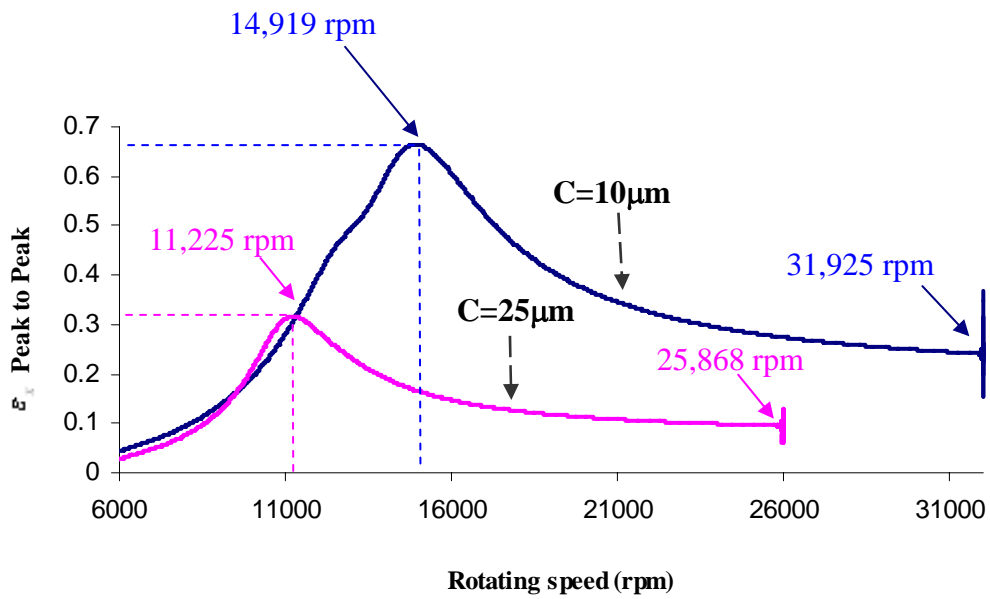
(a) **Simulated** ε_x **peak to peak versus rotating speed**
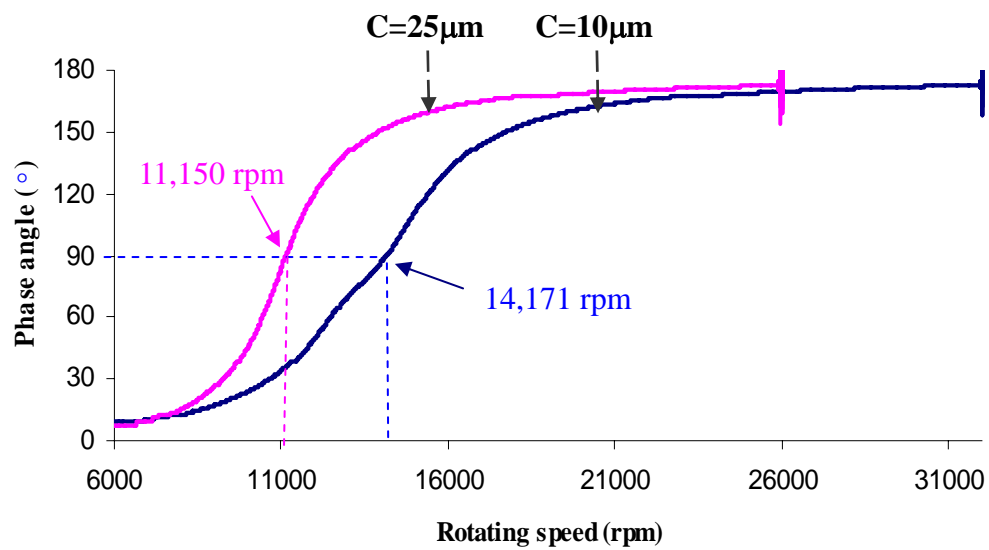
(b) Phase angle versus rotating speed

Figure 4.4 Comparative analytical ε_x peak to peak and phase angle for hybrid bearing with difference bearing clearances; S_f =0.2 and bump stiffness = 0.77 GN/m^3

(a) 16,000rpm

(b) 18,000 rpm

(c) 20,000rpm

(d) 25,000 rpm

(e) 31,000rpm

(f) 35,000 rpm

Figure 4.5 Simulated imbalance response of hybrid bearing at various speeds; C=10μm, supply pressure 400 kPa, bump stiffness = 0.77 GN/m³, γ =0.25

Figure 4.6 depicts a normalized pressure ($P=p/p_a$), film thickness ($H=h/C$), and bump deflection ($W=w_B/C$) for static load of 6N, which corresponds to 0.6kg rotor mass. Note the soft support stiffness (0.77 GN/m^3) renders large bump deflection by the hydrostatic pressurization.
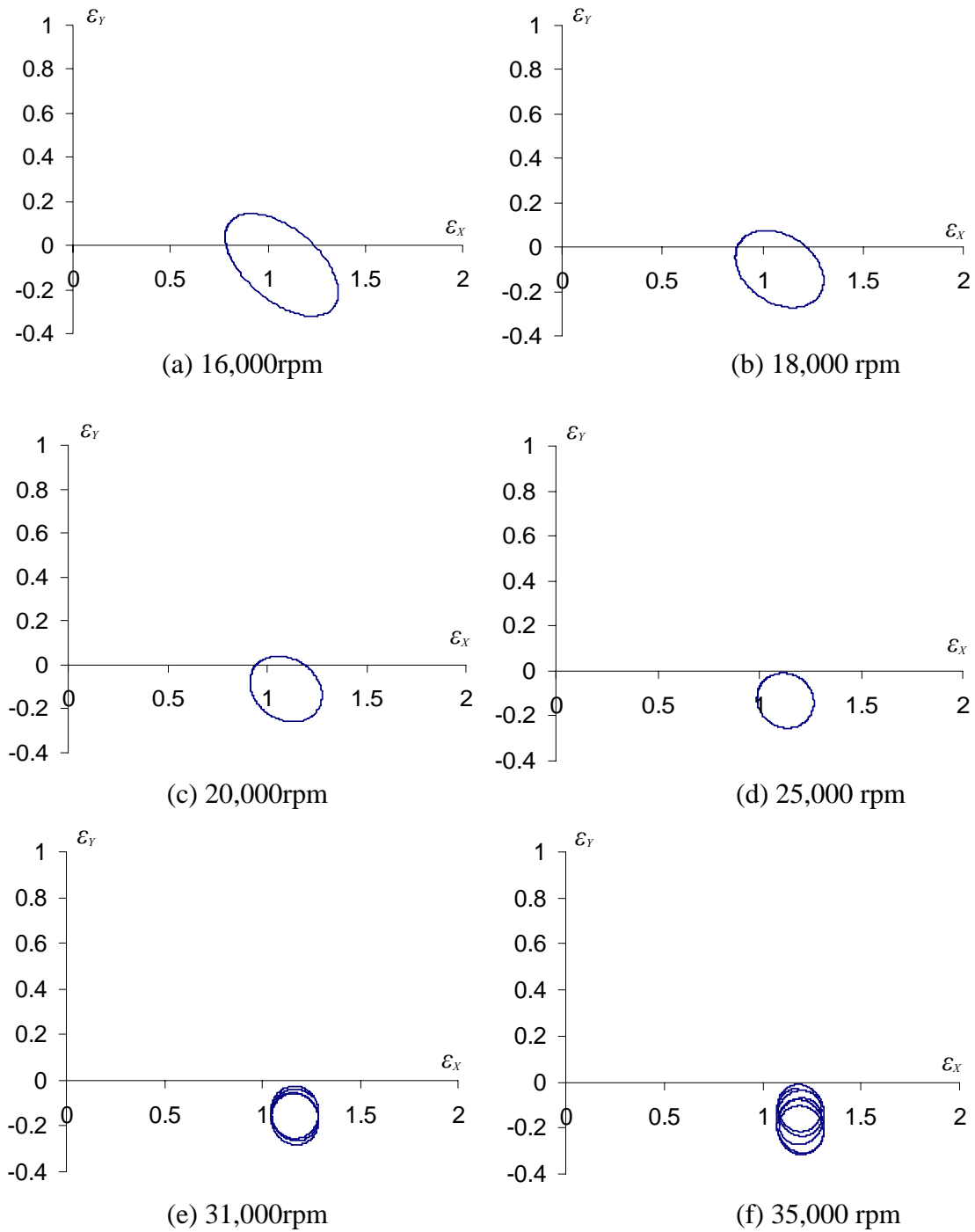
4.3 Effect of Bump Stiffness

This section investigates the effect of the bump spring stiffness on the dynamic performance of hybrid air foil bearing. The manufactured hybrid air foil bearing has very soft bump support compared to commercially available bump foil bearings. Typical bump foil stiffness of 2nd generation bump foil bearings is about 5 GN/m^3. Assuming the same bearing size, simulations were performed with bump stiffness of 5 GN/m^3 and compared with hydrodynamic air foil bearings with the same stiffness and hybrid bearing with softer support. Figure 4.7 is selected orbits at different speeds and Fig. 4.8 is coast down simulation results. From these two figures, the OSI is dramatically increased to 37,040 rpm. From [26], the OSI for the hydrodynamic bearing with bump stiffness of 5 GN/m^3 was about 25,000 rpm.
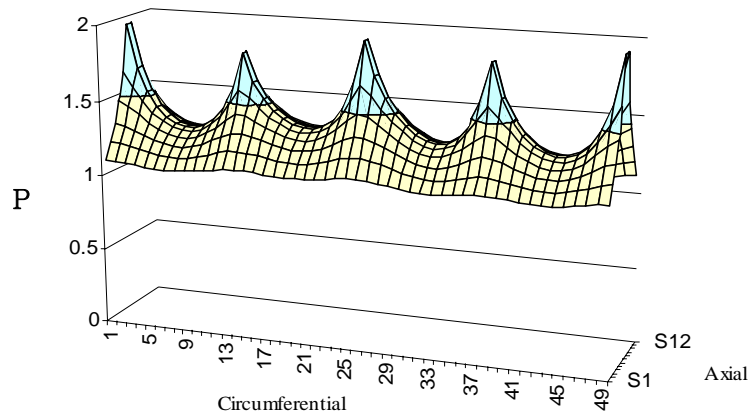
(a) Normalized pressure
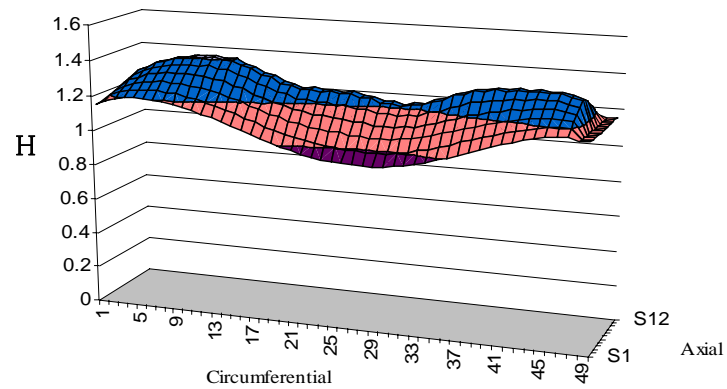
(b) Normalized film thickness
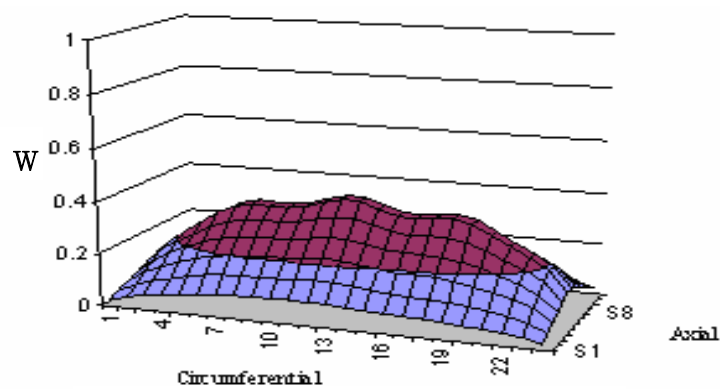
(c) Normalized bump deflection

Figure 4.6 Normalized pressure (P=p/p$_a$), film thickness (H=h/C), and bump deflection (W=w$_B$/C) of hybrid foil bearing

Figure 4.7 Simulated imbalance response at various speeds; C=25μm, supply pressure 400 kPa, bump stiffness = 5 GN/m³, γ =0.25

(a) Simulated ε_x peak to peak versus rotating speed
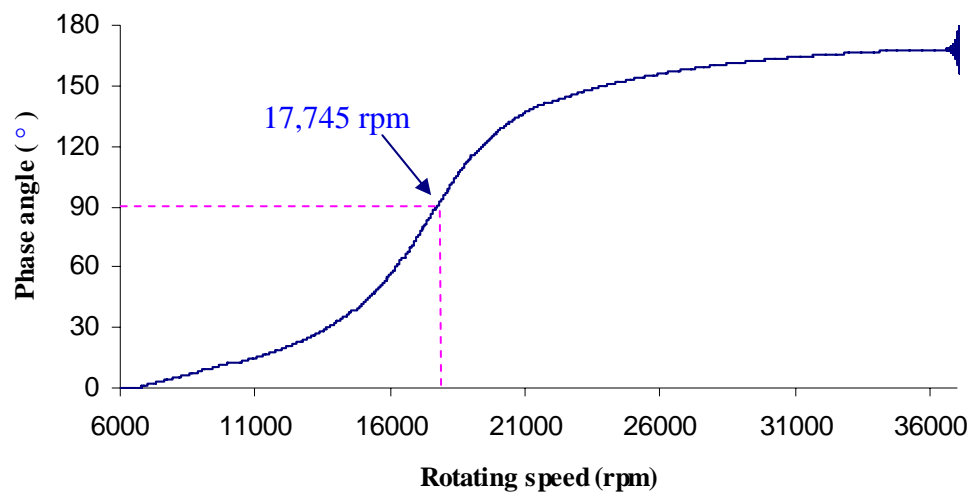
(b) Phase angle versus rotating speed
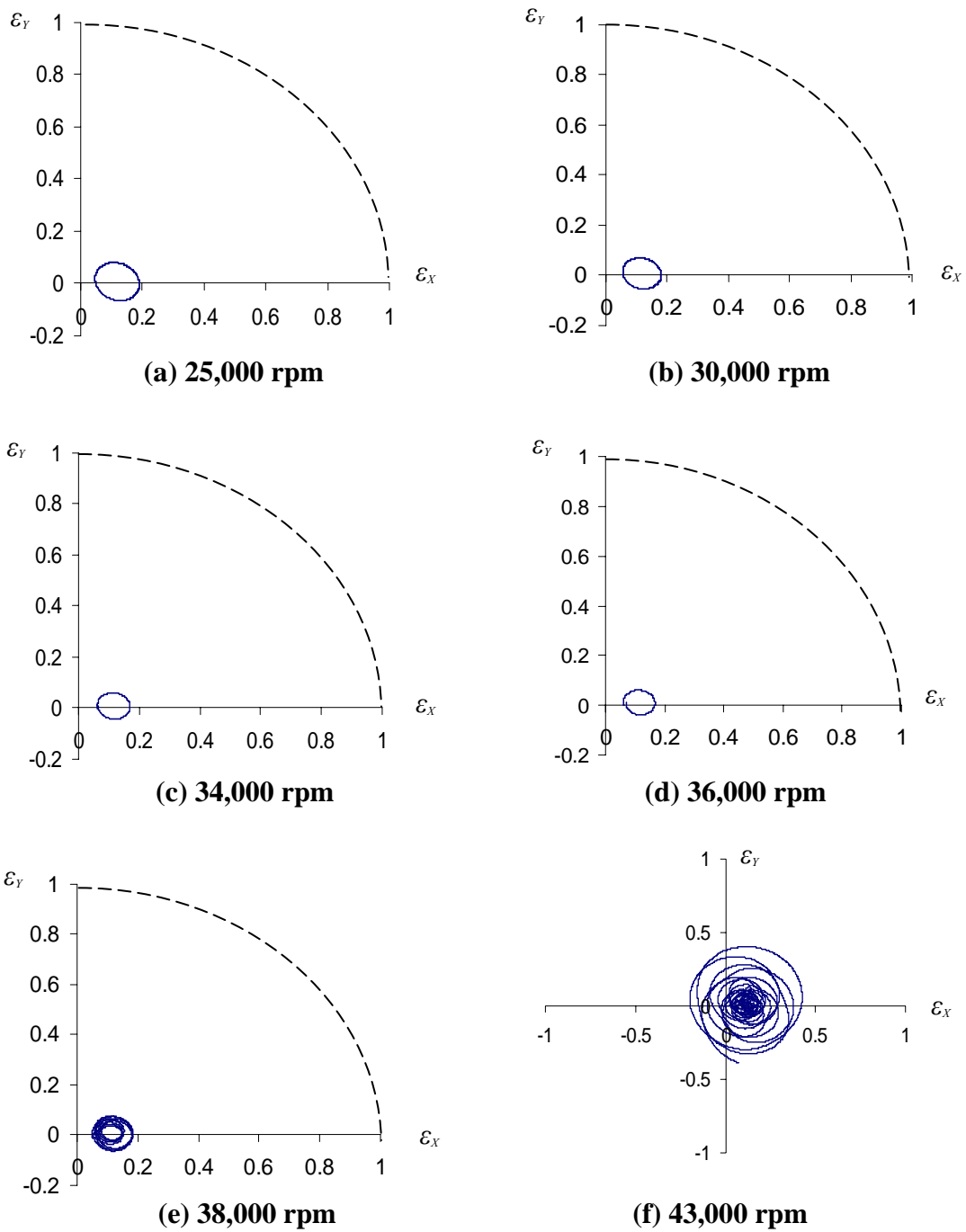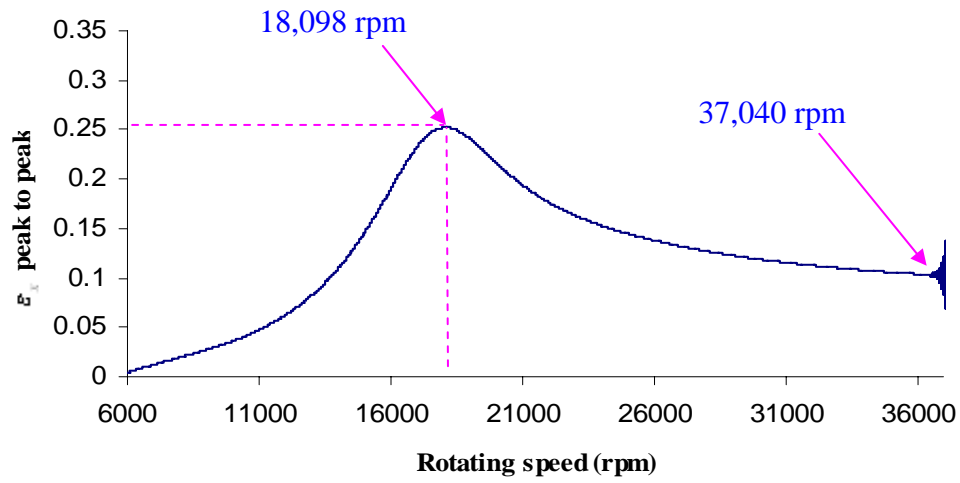
Figure 4.8 Analytical ε_x peak to peak and phase angle of hybrid rotor-bearing imbalance responses with rotating speed; bump stiffness = 5 GN/m³

4.4 Effect of Supply Pressure

Effect of different supply pressure on the dynamic performance of hybrid air foil bearing is investigated in this section. For all the parametric studies, it is assumed that the rotor mass, clearance, and bump stiffness are 0.6kg, 25 μm , and 5 GN/m^3 respectively. The air supply pressure was varied from 300 kPa (44psi) to 600 kPa (87psi) with 100 kPa (14.5psi) increment, and two different (additional) static loads, i.e., 30N and 50N, were compared. Figure 4.9 shows a trend of OSI of hybrid air foil bearing with different air supply pressures for different static loads. As the air supply pressure is increased, the OSI increased. In the similar way, increased load also increased the OSI significantly, manifesting the well-known benefit of loaded-bearings.
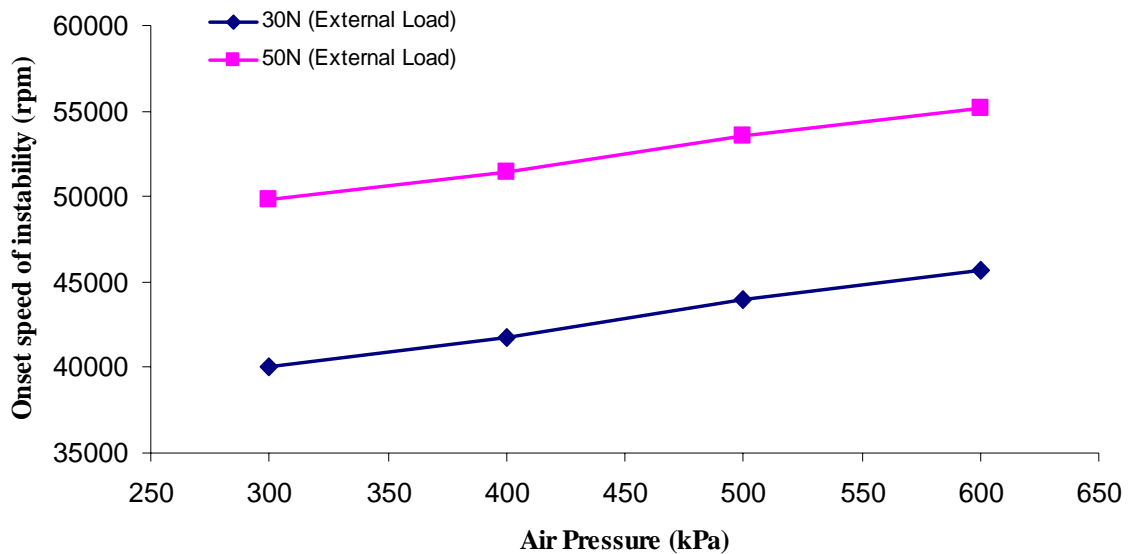
Figure 4.9 Onset speed of instability of hybrid foil air bearing with variable air pressures and external loads; C=25 μm , bump stiffness = 5 GN/m^3

CHAPTER V

EXPERIMENTAL STUDIES

5.1 Load Capacity Measurements

5.1.1 Experimental Setup

In Fig. 5.1 the whole experimental apparatus for measuring load capacity is shown. The test rig consists of three parts, motor, bearing supports, and rotor. The DC motor is operated at 20,000 rpm and connected to the rotor via a flexible coupling. Two ball bearings support the test rotor. The rotor is made of hollow stainless steel shaft with hard Ni on the surface. Two small air jets were used to maintain the constant temperature of ball bearings during the test.
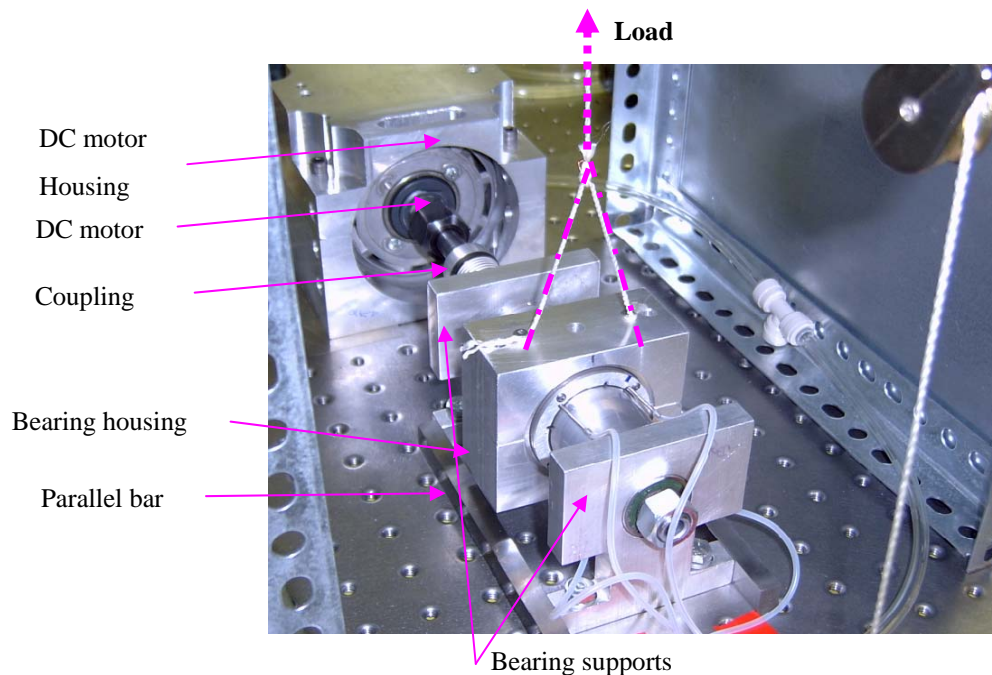
Figure 5.1 Photo of load capacity test rig; test hybrid foil bearing is assembled in the middle of shaft supported by two ball bearings. Vertical load is applied through tension string

(a) General view   **(b) Hybrid bearing with air chamber**
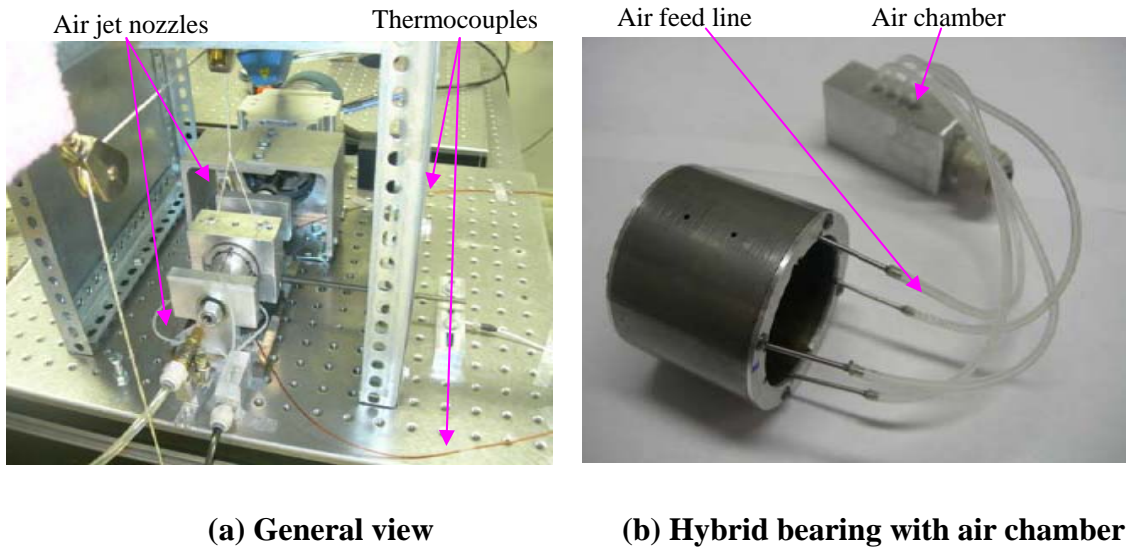
Figure 5.2 Photo of load capacity test rig with air supply chamber

The temperature at loaded area was measured by two thermocouples (Fig. 5.2a), at 0.15 inches from the edge and at the bearing center on the backside of the top foil. Pressurized air was supplied via a 0.042 inch stainless steel tube (Fig. 5.2(b)). Through-flow acrylic panel-mount flow meter measured air flow rate. Four tubes on the backside of the top foil were attached 90° apart along the circumferential direction, as shown in Fig. 2.1. The supply pressure was 276 kPa (40psi). Static loads ranging from 20.4N to 116.6N were applied to the test hybrid air foil bearing via strings. The test conditions for both hydrodynamic operation and hybrid operation are described in Table 5.1. The test conditions for hydrodynamic mode was adopted from [26]

Table 5.1 Test conditions for load capacity measurements

	Hydrodynamic operation	**Hybrid operation**
Operating speed	20.000 RPM	20.000 RPM
Air flow rate	0.085 m^3/minute (3 CFM)	0.0066m^3/minute (0.23 CFM)
Applied loads	15.9, 45.4, 65.8, 76.8, 86.8, 96.3, and 108.6N	20.4, 40.8, 58.3, 68.3, 77.8, 87.2, 96.3, 103.5, 110.2, and 116.6N
Supply pressure	0 Pa (0 bar)	276 kPa (2.76 bar)

Top foil thick.	101.6 mm (4mil)	127 mm (5mil)
Spring stiffness	$0.77\,GN\,/\,m^3$	$0.77\,GN\,/\,m^3$

Figure 5.3 describes the air flow passages for hydrodynamic and hybrid mode. In the hydrodynamic mode,

Distribution channel to plenum chambers

Air supply hole from outside

Plenum chambers that supply air to the holes on the bearing sleeves
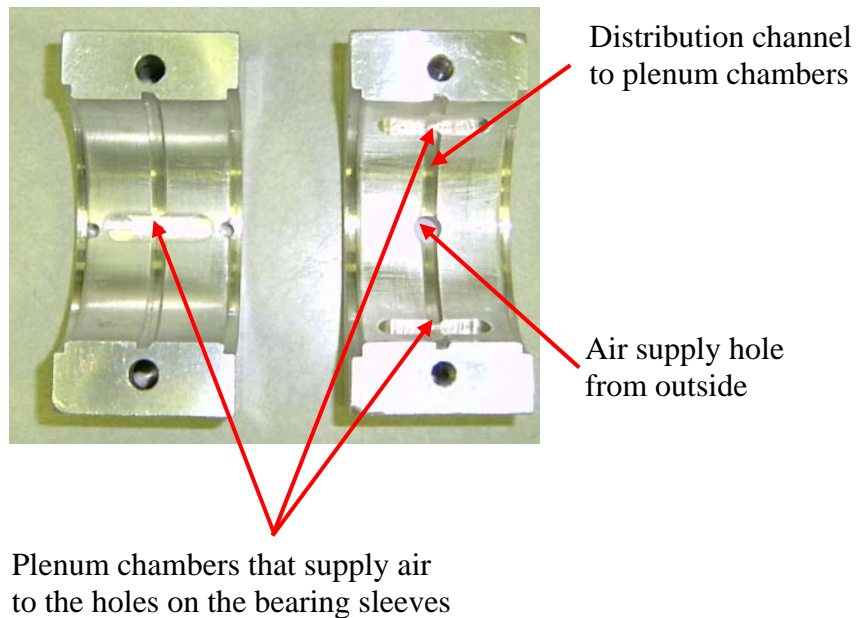
Figure 5.3 Photo of air flow passages: split bearing housing with cooling jacket, surrounding the bearing sleeve[26]

5.1.2 Experimental Results

The hydrodynamic foil bearing with cooling air [26] was used for comparing with hybrid case in views of load capacity and cooling capacity. Contrary to hydrodynamic case, however, the external pressurized air passing through the top foil (Fig. 5.4(b)) was enabled to cool the rotor directly. Experimental studies include measurement of load capacity and cooling performance of the hybrid foil bearing at 20,000 rpm, which is limited by the

current low speed DC motor.

Figure 5.5(a) replots the temperature for the hydrodynamic bearing with cooling air flow rate of 0.085 m^3/min (3cfm) [26]. The maximum temperature increase during the test with maximum load of 96.3N was about 20°C. In hybrid operation, as shown in Fig. 5.5(b), the hybrid bearing was stable until 110.2N. Upon putting 6.4N (116.6N) additionally after 110.2N, the temperature was going to stabilize, but it began to fluctuate suddenly and went above 120°C. The load capacity of hybrid air foil bearing, therefore, was regarded as 110.2N at 276 kPa (40psi) and 20,000 rpm.

From the tests, hybrid operation had higher load capacity and higher cooling capacity with much less air consumption than hydrodynamic operation.

(a) Hydrodynamic cooling air flow   (b) Hybrid air supply flow

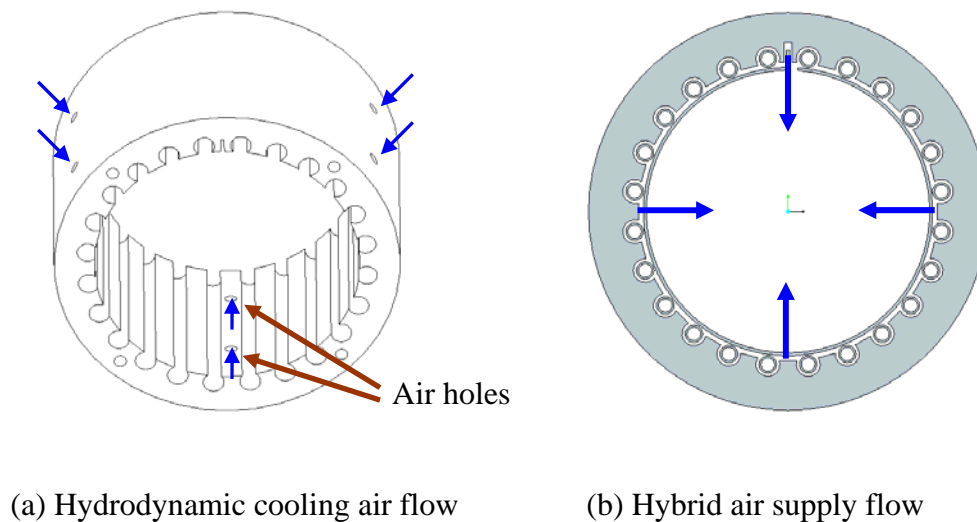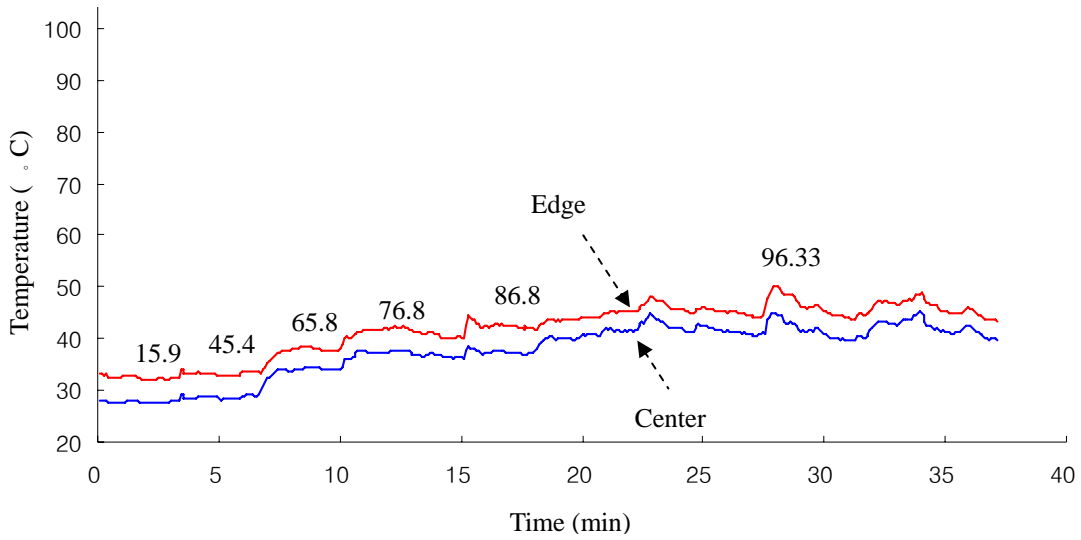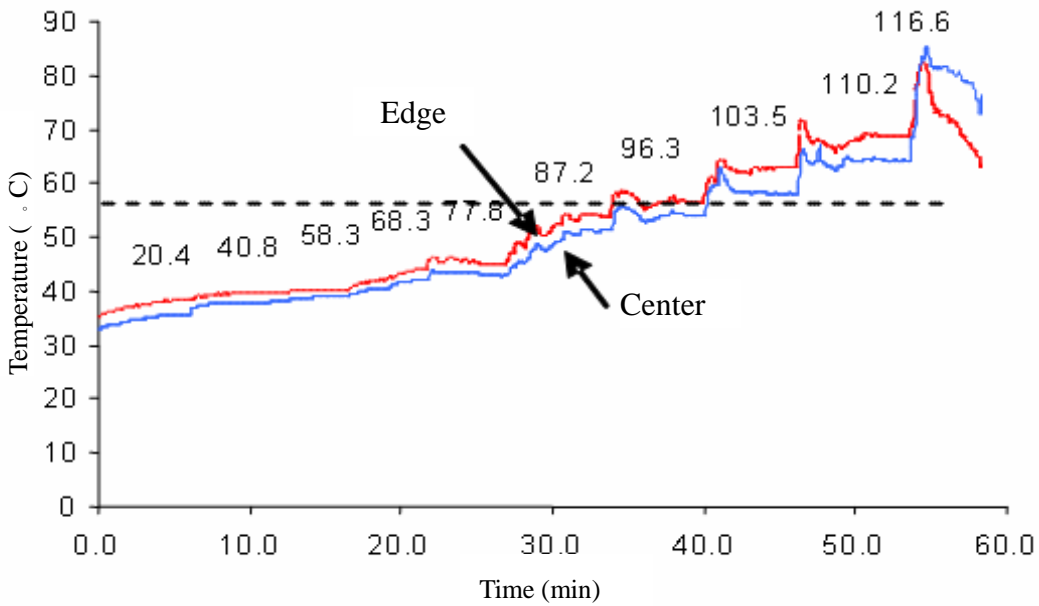**Figure 5.4 Schematic view of cooling system**

(a) Temperature of hydrodynamic operation with cooling air flow rate of 0.085 m^3/min (3cfm) [26]

(b) Temperature of hybrid operation with air flow rate of 0.0066m^3/min (0.233cfm)

Figure 5.5 Bearing temperature with load both hydrodynamic and hybrid operation with spring stiffness 0.77 GN/m^3, numbers represent applied loads in N

The load capacity was also measured with stiffer springs at higher supply pressure Air pressure was increased from 276 kPa (40 psi) to 414 kPa (60 psi), and the original springs were replaced by new springs with higher stiffness of 1.43 GN/m^3, which is twice stiffer than the original one (0.77 GN/m^3). Fig. 5.6 shows the temperature change with applied loads from 20.4N to 116.1N. The temperature rise was about 25°C up to 116.1N, and the load capacity was expected to be larger than the one with softer support. However, upon applying additional 2.8 N, test bearing began to vibrate violently with sharp increase of bearing temperature, leading to complete failure of test bearing. However, considering very stable bearing temperature up to 116.1N, it is highly unlikely that just additional 2.7 N of load failed the test bearing. Even if exact reason for the bearing failure was not known, it was speculated that overall structural problem of the test rig itself caused the failure of the test bearing. Up to 116.1N, the load was applied very carefully to avoid disturbance of the test bearing. However, additional 2.8 N was applied rather suddenly causing initiation of continuous horizontal oscillation of the load string. With the oscillation of the load string, whole test rig began to vibrate and bearing temperature also began to increase sharply. Therefore, the failure of the test bearing at 118.9 N is speculated as overall structural problem of the test rig, rather than problem of test air foil bearing itself. However, visual inspection of the ball bearing support after disassembly of the test rig didn't show any indication of the ball bearing failure.
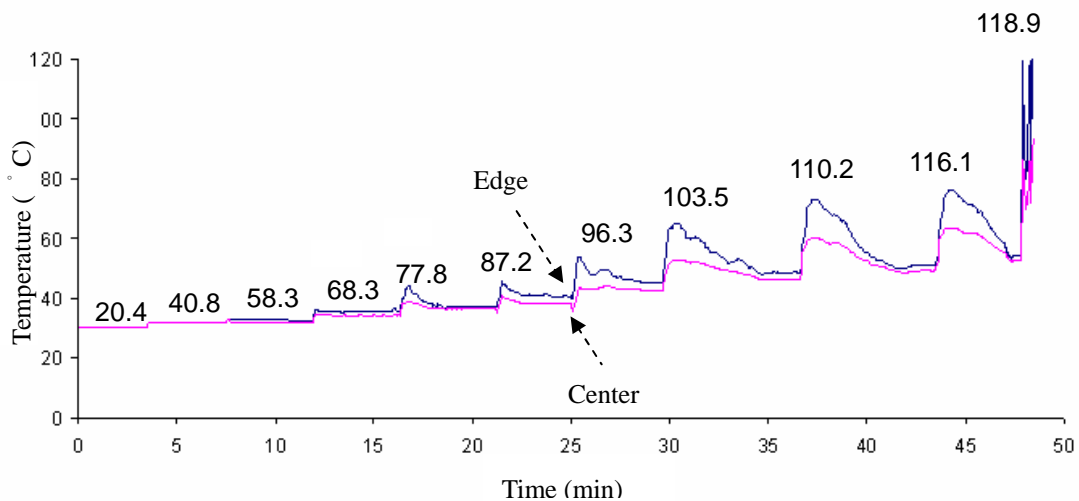

Figure 5.6 Bearing temperatures with external load at 20,000rpm; spring stiffness 1.43 GN/m^3, and air supply pressure 414 kPa (60 psi)

5.2 Torque Measurements

Major benefits of the hybrid foil bearings are very low starting torque, reduced wear of the top foil and rotor, and very effective cooling capability by the pressurized air itself. Friction torques during start/stop were measured and compared with hydrodynamic bearing.

5.2.1 Experimental Setup

Figure 5.7 describes overall configuration of the test rig to measure start torque, and Fig. 5.8 shows photo of the test rig. Due to geometrical constraint in the test rig, the torque rod was attached with slight offset from the bearing center plane as seen in Fig. 5.7. The preload of 6.8N is applied to the load cell through dummy weight m. The test bearing was also loaded with 20.4N to generate high initial friction. The end of the torque rod was connected to the preload and load cell through two tension springs. The moment of inertia of combined mass including the torque rod, bearing housing, and test bearing was 1870.2 $kg \cdot mm^2$. Detailed test parameters, calibrations, and conditions are described in Tables 5.2 and 5.3.
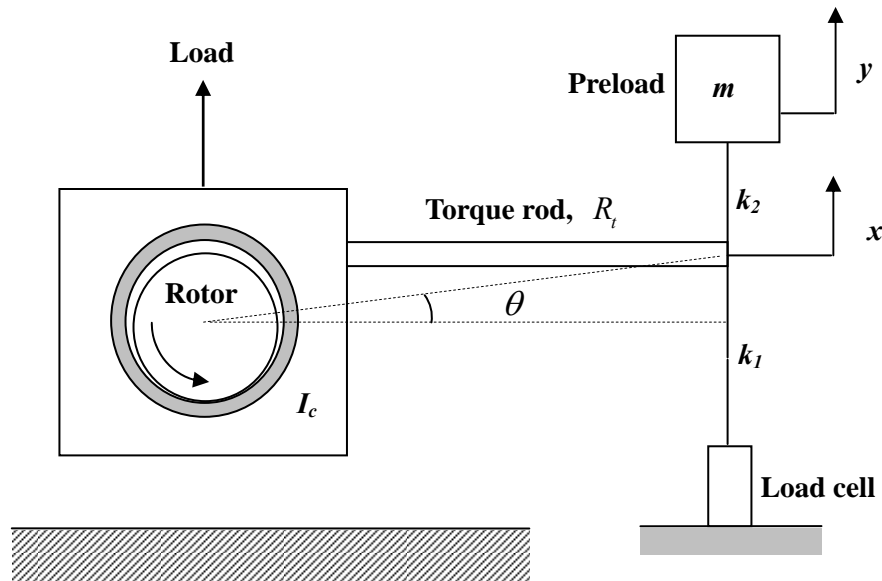
Figure 5.7 Schematic view of torque measurement test rig
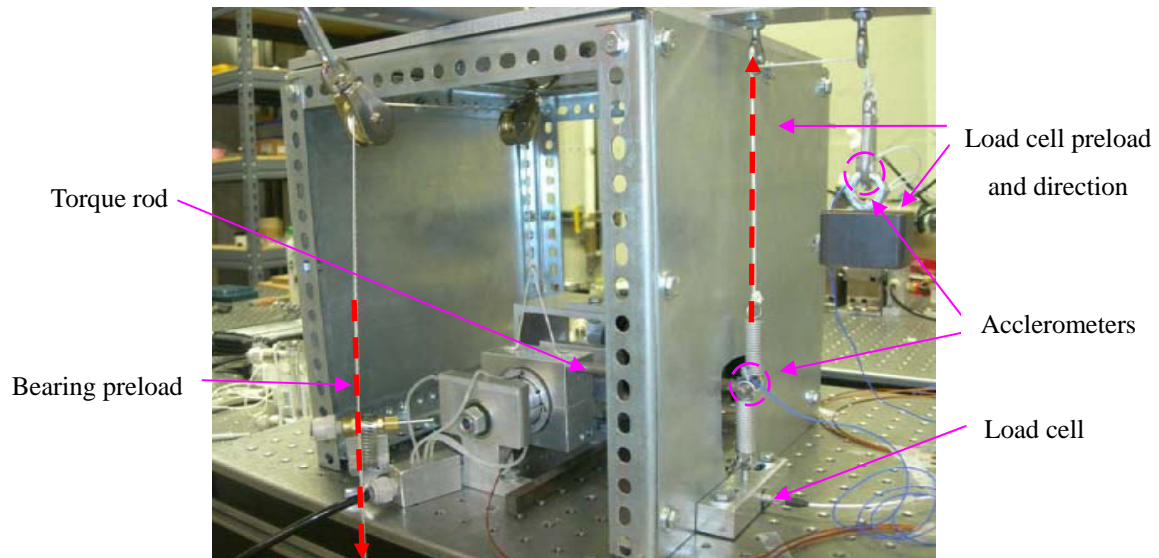
Figure 5.8 Photo of torque measurement rig

Table 5.2 Test parameters and conditions for torque measurement test rig

Length of torque rod		184.65 mm
Moment of Inertia (I)		$1.870 \times 10^3\, Kg \cdot mm^2\,(1.870 \times 10^{-3}\, Kg \cdot m^2)$
Preload	Load cell	6.8 N
	Bearing	20.4 N
Supply air pressure		414 kPa (60 psi)
Air flow rate		0.01 m³/minute (0.35 CFM)
Rotational speed		6,400 rpm

Table 5.3 Calibration data of load cell and accelerometer

F_L	Signal 1	Load Cell (PCB Piezotronics : Model 201B02)	10.89 mV/N
x	Signal 2	Acclerometer 1 (PCB Piezotronics : Model 352B10)	9.78 mV/g
y	Signal 3	Acclerometer 2 (PCB Piezotronics : Model 352B10)	9.81 mV/g

Because the shaft is not perfectly circular and there is a vibration input from the spinning rotor, dynamic inertia forces of the torque rod assembly should be measured and removed from the load cell signal. From Fig. 5.7, the rotational equation of motion of the torque rod assembly can be written by

$$I_c\ddot{\theta} = \tau_f(t) + R_t k_2(y-x) - k_1 x R_t, \tag{28}$$

where I_c is the rotational moment of inertia of torque rod assembly including bearing housing and bearing, θ is the angle of rotation in radians, τ_f is the friction torque from the test bearing , R_t is the length of torque bar from the bearing center, and k_1 and k_2 are spring stiffnesses.

Equation of motion for the mass m and the force to the load cell F_L are given by

$$m\ddot{y} = -k_2(y-x) \tag{29a}$$
$$F_L = k_1 x, \tag{29b}$$

where $x = R_t\theta$. Inserting Eq. (29) into Eq. (28) and rearranging, the expression for the friction torque becomes

$$\tau_f(t) = I_c\ddot{\theta} + mR_t\ddot{y} + F_L R_t = I_c\frac{\ddot{x}}{R_t} + mR_t\ddot{y} + F_L R_t \tag{30}$$

From Eq. (30), acceleration at the tip of the torque rod and preload mass, m should

be measured using accelerometers and added to the load cell signal F_L to find true friction torque from the test bearing.

5.2.2 Experimental Results

Due to the flexibility and precision error of the top foil, the bearing did not fully lift off even under hydrostatic pressurization, i.e., several local high spots still made a dry contact with the rotor. However, when static load of about 20.4N was applied, the bearing friction became smaller. The test was performed at 6,400 rpm. Measured signal was stored for about 15 seconds, 5 seconds before motor starts, 5 seconds of motor running at 6,400 rpm, and additional 5 seconds after motor stopped.

Figure 5.7 shows raw data of friction torque, i.e., $F_L R_t$, before adding inertia terms. As can be seen, the raw data does not show meaningful information on true friction torque. Figure 5.8 is a true friction torque, $\tau_f(t)$, after adding the two inertia terms in Eq. (30). In hydrodynamic operation, during start and stop, dry sliding contact of the rotor against the bearing produced the maximum friction torque of about 100*N-mm*. In hybrid operation, the lifted rotor rotates without contacting bearing surface and the initial friction between the bearing surface and the rotor is quite small as shown in Fig. 5.8(b). There was no visible wear on the bearing and rotor surfaces during start and stop.
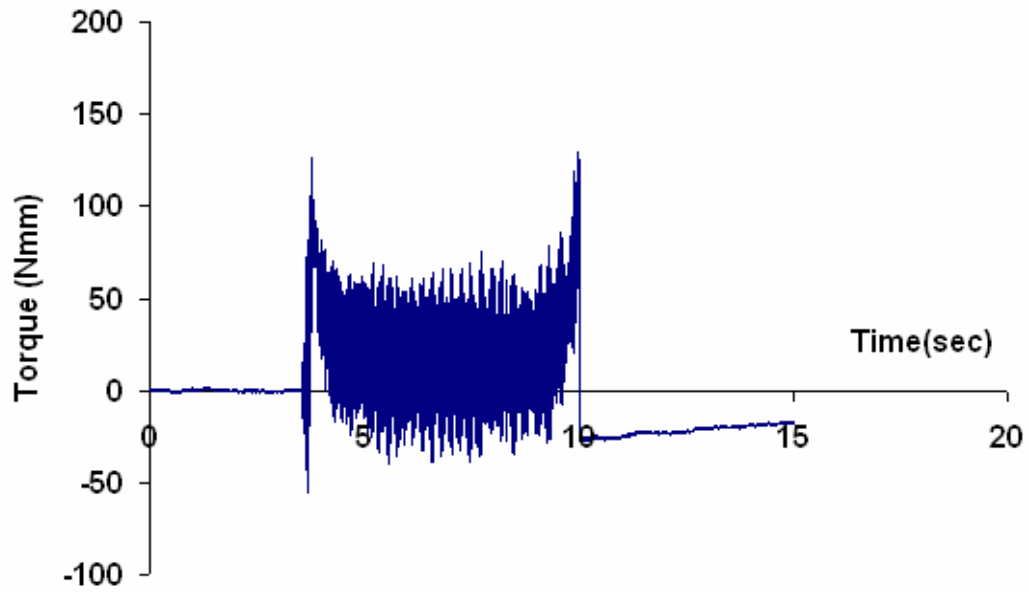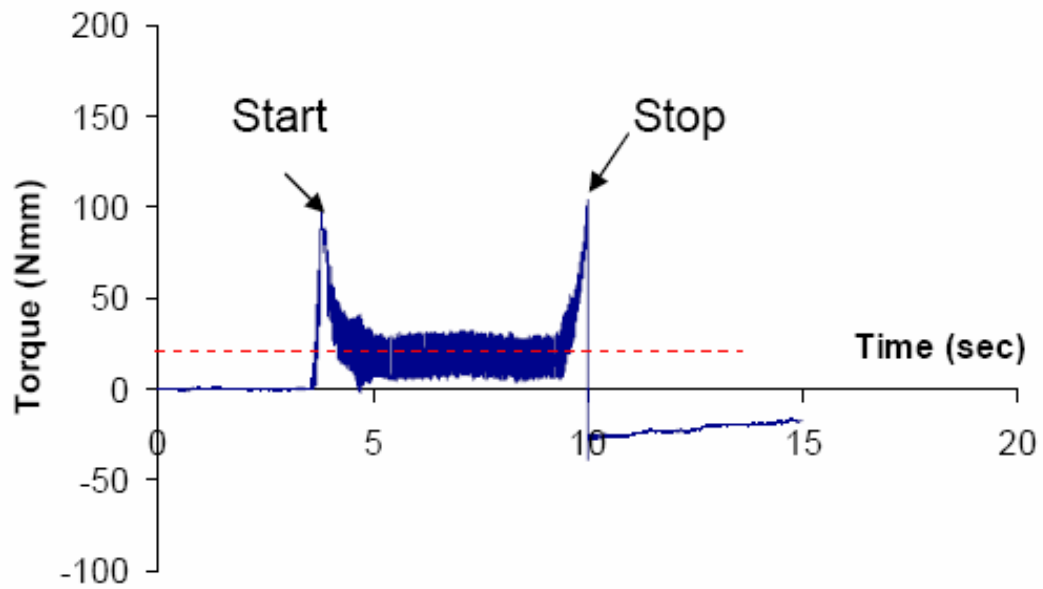
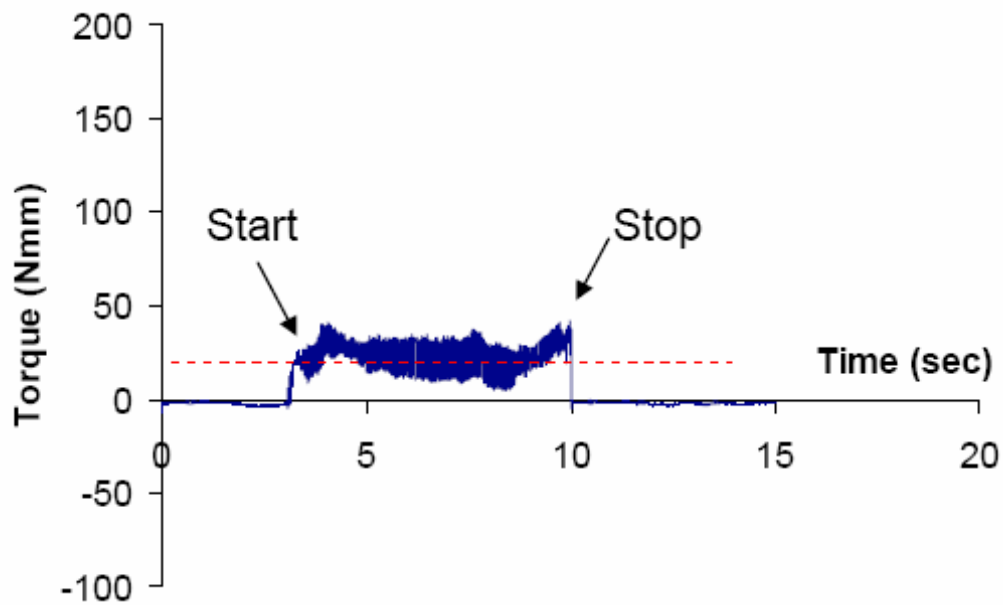**(a) Starting torque in hydrodynamic operation**
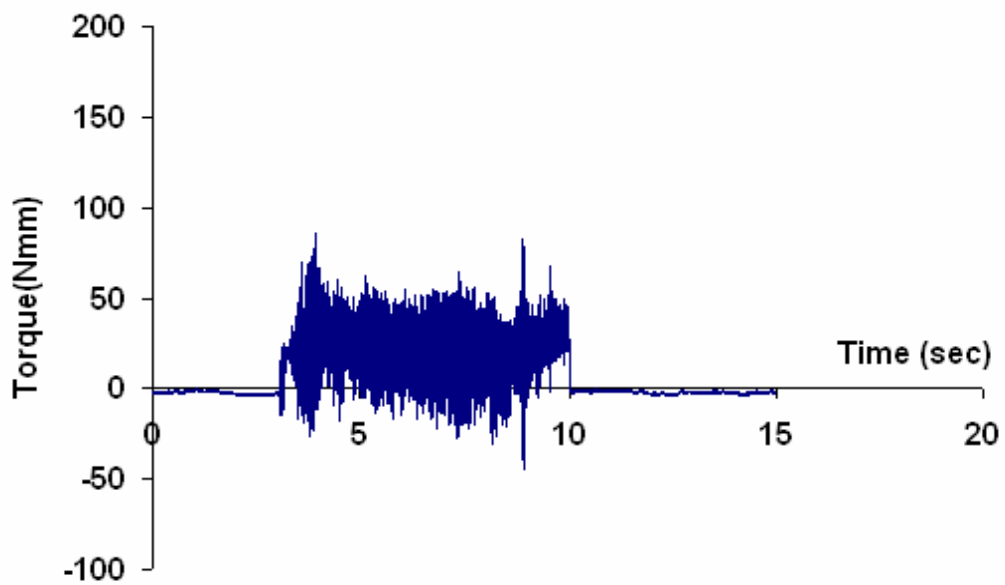
(b) Starting torque in hybrid operation

Figure 5.9 The raw data of starting friction torque F_LR_t

(a) Starting torque in hydrodynamic operation

(b) Starting torque in hybrid operation

Figure 5.10 Starting friction torque after compensation of inertia forces

CHAPTER VI

CONCLUSION

The hybrid air foil bearing was designed and constructed for the first time in order to reduce wear issues and provide higher load capacity and stability.

To achieve a realistic top foil deflection in hybrid operation, sagging effect on the top foil was implemented through analytical 1-D beam model. Developed model showed very good agreement with available experimental data. The orbit simulation method was applied to predict imbalance responses, i.e., critical speed and onset speed of instability of hybrid air foil bearings. Predictions indicate the hybrid air foil bearings can have much higher onset speed of instability. To the contrary to the hydrodynamic bearing, smaller clearance yielded higher onset speed of instability in hybrid operation, manifesting beneficial effect of air injection which disturbs circumferential air flow. Parametric studies were performed in terms of bump stiffness and supply pressure. It showed that higher onset speeds of the instability could be achieved by increasing the stiffness of the spring and air supply pressure.

Load capacity of hybrid air foil bearing was measured and compared with hydrodynamic bearing. Higher load capacity with much less air consumption was observed than hydrodynamic bearing. Much less air consumption than hydrodynamic bearing is a noticeable advantage of hybrid air foil bearing in terms of efficiency and cooling capacity. Considering direct injection of air can cool both air film and rotor, thermal distortion of the rotor can be minimized. Thermal distortion and/or expansion of the rotor have also been a cause of foil bearing failure in many applications. In addition, start torque while the bearing is loaded was very small, being comparable to the friction at steady state operation. The small start torque clearly indicates that the hybrid air foil bearing can eliminate wear problems which has been a chronic failure mode of heavily loaded air foil bearing.

REFERENCES

[1] Agrawal, G. L., 1997, "Foil Air/Gas Bearing Technology-An Overview," ASME Paper 97-GT-347.

[2] Costamagna, P., Magistri, L., and Massardo, A. F., 2001, "Design and Part-Load Performance of a Hybrid System Based on a Solid Oxide Fuel Cell Reactor and a Micro Gas Turbine," ASME Journal of Power Sources, **96**, pp. 352-368.

[3] NASA, March 2006, *NASA FactSheet,*
http://www.nasa.gov/centers/glenn/about/fs14grc.html

[4] Ku, C.-P. and Heshmat, H., 1992, "Compliant Foil Bearing Stuctural Stiffness Analysis: Part I-Theoretical Model Including Strip and Variable Bump Foil Geometry," ASME Journal of Tribology, **114**, pp. 394-400.

[5] Ku, C.-P. and Heshmat, H., 1993, "Compliant Foil Bearing Structural Stiffness Analysis: Part II-Theoretical Model Including Strip and Variable Bump Foil Geometry," ASME Journal of Tribology, **115**, pp. 364-369.

[6] Heshmat, H. and Ku, C.-P., 1994, "Structural Damping of Self-Acting Compliant Foil Journal Bearings," ASME Journal of Tribology, **116**, pp. 76-82.

[7] Peng, J. P. and Carpino, M., 1993, "Calculation of Stiffness and Damping Coefficients for Elastically Supported Gas Foil Bearings," ASME Journal of Tribology, **115**(1), pp. 20-27.

[8] Heshmat, C. A., Xu, D. S., and Heshmat, H., 2000, "Analysis of Gas Lubricated Foil Thrust Bearings Using Coupled Finite Element and Finite Difference Methods." ASME Journal of Tribology, **122**, pp. 199-204.

[9] Peng, Z-C. and Khonsari, M., 2006, "A Thermohydrodynamic Analysis of Foil Journal Bearings," ASME Journal of Tribology, **128**, pp. 534-541.

[10] DellaCorte, C. and Valco, M. J., 2000, "Load Capacity Estimation of Foil Air Journal Bearings for Oil-Free Turbo-Machinery Applications," STLE Tribology Transactions, **43**(4), pp. 795–801.

[11] Kim, T. and San Andrés, L., 2005, "Heavily Loaded Gas foil Bearings: A Model Anchored to Test Data," ASME Paper GT2005-68486.

[12] Kim, D., 2006, "Parametric Studies on Static and Dynamic Performance of Air Foil Bearings with Different Top Foil Geometries and Bump Stiffness Distributions," In press to ASME Journal of Tribology.

[13] San Andrés, L. and Kim, T. H., 2006, "Computational Analysis of Gas Foil Bearings Integrating 1D and 2D Finite Element Models for Top Foil," Technical Report No TRC-B&C-1-06, Texas A&M Univ., College Station, TX.

[14] Lee, D.–H., Kim, Y.-C., and Kim, K.-W., 2004, "The Static and Dynamic Performance Analyses of Air Foil Journal Bearings for Various Bump Foil Stiffness," J. KSTLE, **20**(5), pp. 245-251.

[15] Carpino, M. and Talmage, G., 2003, "A Fully Coupled Finite Element Formulation for Elastically Supported Foil Journal Bearings," Tribology Transactions, **46**, pp 560-565.

[16] Heshmat, H., Walowit J. A., and Pinkus, O., 1983, "Analysis of Gas-Lubricated Foil Journal Bearings," ASME J. Lubr. Technol., **105**, pp. 647–655.

[17] Carpino, M., Medvetz, L.A., and Peng, J.P., 1993, "Effects of Membrane Stresses in the Prediction of Foil Bearing Performance," Tribology Transactions, **37**, pp. 43-50

[18] Ruscitto, D., Mc Cormick, J., and Gray, S., 1978, "Hydrodynamic Air Lubricated Compliant Surface Bearing For An Automotive Gas Turbine Engine I-Journal Bearing Performance," NASA CR-135368.

[19] Salehi, M., Heshmat, H., and Walton, J. F., 2003, "On the Frictional Damping Characteristics of Compliant Bump Foils," ASME Journal of Tribology, **125**, pp. 804-813.

[20] Heshmat, H., 1994, "Advancements in the Performance of Aerodynamic Foil Journal Bearings: High Speed and Load Capacity," ASME Journal of Tribology, **116**, pp. 287-295.

[21] Radil, K., Howard, S., and Dykas, B., 2002, "The Role of Radial Clearance on the Performance of Foil Air Bearings," STLE Tribology Transactions, **45**(4), pp. 485–490.

[22] Capstone Turbine Corporation, March 2007, *Capstone MicroTurbine,* http://www.microturbine.com

[23] DellaCorte, C. and Edmonds, B. J., 1995, "Preliminary Evaluation of PS300: A New Self-Lubricating High Temperature Composite Coating for Use to $800^{\circ}C$, NASA Technical Report NASA TM-107056.

[24] Stanford, M. K., Yanke, A. M., and DellaCorte, C., 2004, "Thermal Effects on a Low Cr Modification of PS304 Solid Lubricant Coating, NASA Technical Report NASA TM-2003-213111.

[25] Mohawk Innovative Technology, 2005, "Low-Friction, Wear-Resistant Korolon™ Coatings for High-Temperature, High-Speed, Air Foil Bearings," Mohawk Innovative Technology Internal Newsletter, 23, Albany, NY.

[26] Song, J. and Kim, D., 2006, "Foil Bearing with Compression Springs: Analyses and

Experiments″ Accepted to ASME Journal of Tribology.

[27] Timonshenko, S., 1983, *Strength of Materials, Part 1 and Part 2* (3rd edition), Krieger Pub Co., Malabar, FL.

[28] D. Han, S. Park, W. Kim, J. Kim, 1994, "A Study on the Characteristics of Externally Pressurized Air Bearings," Precision Engineering, **16(3)**, pp. 164-173.

[29] Nikrayesh, P.E., 1988, *Computer-Aided Analysis of Mechanical Systems*, Prentice Hall, Upper Saddle River, NJ.

[30] Iordanoff, I. 1999, "Analysis of an Aerodynamic Complaint Foil Thrust Bearing: Method for a Rapid Design," ASME Journal of Tribology, **121**, pp. 816-822.

VITA

Soongook Park was born in 1979 in Daegu, The Republic of Korea. He received a B.S. in Electrical Engineering from the Korea Military Academy in 2002, then he was commissioned as a Transportation officer. He served in the ROK Army from 2002 to 2004 as a platoon leader and staff officer. He entered the Mechanical Engineering Department at Texas A&M University in 2005 as an M.S. student and graduated in May 2007.

Permanent Address: Department of Mechanical Engineering, 3123, TAMU,
College Station, Texas, 77843-3123, USA.

Chair of Committee: Dr. Daejong Kim

E-mail Address: soongugi@hotmail.com